Monthly Notices
of the
ROYAL ASTRONOMICAL SOCIETY

MNRAS **449,** 3021–3042 (2015) doi:10.1093/mnras/stv466

Investigating early-type galaxy evolution with a multiwavelength approach – I. X-ray properties of 12 galaxies observed with *Swift* and *XMM–Newton*

G. Trinchieri,[1⋆] R. Rampazzo,[2] P. Mazzei,[2] A. Marino[2] and A. Wolter[1]

[1]*INAF–Osservatorio Astronomico di Brera, via Brera 28, 20121 Milano, Italy*
[2]*INAF–Osservatorio Astronomico di Padova, Vicolo dell'Osservatorio 5, 35122 Padova, Italy*

Accepted 2015 March 2. Received 2015 March 2; in original form 2014 November 4

ABSTRACT

We report here the results from the X-ray observations of 12 early-type galaxies (ETGs) observed with *Swift* and *XMM–Newton*, originally selected from a sample of galaxies with *Spitzer* and/or *GALEX* data. With the combined analysis of new X-ray and optical–UV observations and of previously available data from archives, we aim at investigating the relation between X-ray luminosity and evolutionary phases of ETGs. We will interpret the results with the additional aid of smoothed particle hydrodynamics chemo-photometric simulations. All galaxies have been detected in the X-ray band, with luminosities $L_{\rm x} > 10^{39}$ erg s^{-1}. X-ray emitting gas has been detected in about half of the sample, with luminosities from $\geq 10^{39}$ to 10^{40} erg s^{-1}. UVOT images show a variety of morphologies, from absence of peculiar features relative to optical wavelengths typical of red and dead early-types, to well defined almost circular rings clearly emerging in the *U* band, to more spectacular and complex features connected to recent or even ongoing star formation (SF). We find little evidence of any influence of the SF activity on their global X-ray properties, and in particular, on the luminosity-weighted age of the system, usually estimated in the nuclear region. However, with the present data we cannot exclude that such a relation exists on smaller scales, related to the specific sites where we see evidence of newly formed stars, such as outer rings and arcs and peculiar features observed in UV images.

Key words: galaxies: elliptical and lenticular, cD – galaxies: evolution – galaxies: formation – ultraviolet: galaxies – X-rays: galaxies.

1 INTRODUCTION

Nearby early-type galaxies (ETGs) are the fossil record of galaxy evolution. Progress in understanding their detailed properties is then essential to pinpoint and constrain the final stages of their evolution and retrace their history.

Most ETGs (elliptical and lenticular galaxies) are assumed to be primarily composed of old, low-mass stars, with limited amounts of cold interstellar medium (ISM), insufficient to sustain or feed ongoing star formation (SF) activity. In the last decades, particular effort has been dedicated to *timing* the ETGs evolution through the parameter 'age', namely the average luminosity-weighted age (plus metallicity and α-enhancements) of their stellar component, estimated through optical spectroscopic indices coupled with suitable stellar population modelling (see e.g. Annibali et al. 2007, and references therein). This effort, combined with kinematical and multiband structural analysis of ETGs, lead to the conclusion that episodes of SF, rejuvenating the stellar populations, are not rare in these fossil galaxies, presumably triggered by interaction, accretions and merging episodes (Longhetti et al. 2000, and references therein).

With the *Spitzer Space Telescope*, the mid-infrared (MIR) window allowed the identification of ETGs with passively evolving spectra (Bressan et al 2006) and those with ongoing SF in their nucleus (see e.g. Panuzzo et al. 2011; Rampazzo et al. 2013, and references therein), identified e.g. by polycyclic aromatic hydrocarbon (PAH) in their central regions, although with anomalous ratios (Kaneda et al. 2008; Panuzzo et al. 2011; Rampazzo et al. 2013) relative to star-forming galaxies. Vega et al. (2010) suggest that these anomalous PAHs are produced by carbon stars a few Gyr old present in the stellar populations (Nanni et al. 2013, see their table 1), on average formed about $z \lesssim 0.2$, depending on the metallicity. The MIR spectra of the nuclei have been interpreted as a snapshot of an accretion episode (Panuzzo et al. 2011) superposed on a passively evolving spectrum (see their fig. 11).

Passive evolution implies that gas lost from the evolving stars over several gigayears accumulates in ETGs and can be heated

⋆ E-mail: ginevra.trinchieri@brera.inaf.it

Table 1. The sample of ETGs.

Ident.	Morpho. RSA	Opt.[a] class	MIR class	Dist (Mpc)	Scale (kpc arcsec^{-1})	$P_{1.4\,\mathrm{GHz}}$ (W Hz^{-1})	log L_K ($L_{K\odot}$)	L_X^a (LMXB)	L_X^a (CV+AB)
NGC 1209	E6	LIN(H)	1	35.8 ± 3.6	0.169	1.9×10^{21}	11.09	40.09	39.06
NGC 1366	$S0_1(8)$	IN	1	21.1 ± 2.1	0.100	–	10.35	38.07	37.05
NGC 1415[b]	Sa/SBa late	–	–	22.7 ± 1.5	0.109	9.7×10^{20}	10.70	39.70	38.68
NGC 1426	E4	IN	0	24.1 ± 2.4	0.117	$<8.5 \times 10^{19}$	10.60	39.60	38.58
NGC 1533	$SB0_2(2)$/SBa	LIN(H)	2	21.4 ± 2.1	0.103	–	10.91	39.34	38.32
NGC 1543	$RSB0_{2/3}(0)$/a	–	–	20.0 ± 2.0	0.097	–	10.93	39.93	38.91
NGC 2685	$S0_3(7)$ pec	S2/T2	2	16.0	0.080	5.6×10^{19}	10.37	39.37	38.35
NGC 2974	E4	LIN(H)	2	21.5 ± 2.2	0.103	5.7×10^{20}	11.48	40.48	39.46
NGC 3818	E5	IN(Traces)	0	36.3 ± 3.6	0.174	$<2.810^{20}$	10.89	39.89	38.87
NGC 3962	E1	LIN(H)	2	35.3 ± 3.5	0.169	$1.6\ 10^{21}$	11.34	40.34	39.31
NGC 7192	$S0_2(0)$	LIN(W)	1	37.8 ± 3.8	0.179	–	11.06	40.06	39.03
IC 2006	E1	Comp(W)	1	20.2 ± 2.0	0.097	4.9×10^{19}	10.53	39.53	38.50

Notes. Opt. Class: same notation as in Annibali et al. (2010) – LIN = LINER; AGN = AGN like emission; IN = either faint (Traces) or no emission lines; Comp = transition between H II regions and LINERs. W and H indicate weak emission (EW(α + [N II]6584) < 3Å) and strong emission line galaxies, respectively. The classification of NGC 2685 is derived from Ho, Filippenko & Sargent (1997) where S is for Seyfert and T from transition object.
MIR class from Rampazzo et al. (2013).
Dist from The Extragalactic Distance Database (EDD): http://edd.ifa.hawaii.edu/.
Radio power at 1.4 GHz, $P_{1.4\,\mathrm{GHz}}$ from Brown et al. (2011), or Condon et al. (1998), rescaled to the adopted distances. L_K is derived from the total K magnitudes from the 2MASS survey at http://irsa.ipac.caltech.edu/Missions/2mass.html, adopting $M_K = 3.28$ for the Sun.
[a]Contribution from LMXB and AB+CV sources to the 0.3–8.0 keV luminosity in erg s^{-1} (calculated as in Boroson, Kim & Fabbiano 2011).
[b]Classified (R)SAB(s)0/a in RC3 (see also Table 2).

at a temperature of $\gtrsim 10^6$ K, emitting in the X-ray band through continuum thermal and metal line emission. The detailed properties of this gas, and in particular the link with other characteristics of the ETGs and their evolution, have been the subject of investigation for many years. ETGs with similar optical luminosities and age might be expected to have similar X-ray luminosities, since a comparable amount of mass should be released into the ISM from similar stellar populations. However, the surprisingly large dispersion in the X-ray versus optical luminosity relation first known since the *Einstein Observatory* data (e.g. Forman, Jones & Tucker 1985; Trinchieri & Fabbiano 1985) have partially been better understood, and reduced at the high-luminosity end, by selecting the samples appropriately and more homogeneously, and by more accurate measures of the X-ray components, but it has not been fully solved at the present time. Two main reasons are at the basis of this lack of knowledge: (1) a comprehensive investigation of the actual evolutionary phase of an ETG, e.g. the time-scales of the phenomena driving its current/past evolution, from accretion to SF, from an active galactic nucleus (AGN) phase to the feedback, is only a recent and still ongoing project; (2) in spite of repeated efforts, a multiwavelength cover of a suitable (at least representative, better complete) sample of ETGs with hot gas are still mostly limited to the brighter, gas-richer examples.

This is the first paper of a series dedicated to the study of the relation between the X-ray content and the evolution of ETGs. We plan to use original and archival observations as well as smoothed particle hydrodynamics (SPH) simulations with chemo-photometric implementation to investigate if and to what extent the X-ray emission is connected to ETGs evolution driven by accretion and/or feedback episodes.

Brassington, Ponman & Read (2007) suggest that the X-ray content of merging galaxies may vary significantly when a merging event occurs. In particular they indicate that mergers at very early stages are significantly fainter in X-rays than normal mature systems in which they will evolve. The effect on minor mergers and/or accretion events between gas-poor ETGs and smaller gas-rich satellites is most likely less evident, but could be, at least qualitatively, consistent with the major merger picture (cf. Trinchieri et al. 2008)

We are then using MIR *Spitzer*-IRS spectroscopy of the nuclear region and *GALEX* far-UV (FUV) images to identify tracers of the SF history of ETGs, in particular of the more recent event (see Rampazzo et al. 2014), connected to interaction/accretion/merging. As shown by Rampazzo et al. (2013), MIR spectra and morphological and kinematical peculiarities indicate whether these phenomena are in action. In this paper we will discuss objects with MIR nuclear spectra characterizing either a quiescent phase (MIR class 0/1) or one just after a recent event (class 2) that has modified the spectral characteristics of the nuclear region. The FUV images highlight ongoing SF in ring/arm-like structures in about half of the present sample, further indicating the complexity of the interaction/accretion phenomena going on (cf. Mapelli, Rampazzo & Marino 2015).

We aim at understanding whether and in what way the global X-ray emission is affected by what has happened, and whether the X-ray emission of quiescent ETGs differs from that of those that show a recent activity.

We use a set of ETGs, mostly S0s with a clear signature of interaction/accretion episodes, for which we have obtained X-ray and FUV imaging using the *Swift* satellites (XRT and UVOT instruments) and *XMM–Newton*. We use the distances and main optical parameters quoted in Table 1. Uncertainties quoted in table for the spectral parameters are at the 90 per cent confidence level for two free parameters. The sample includes galaxies located in very low and intermediate density environments, $0.13 \leq \rho_{xyz} \leq 0.95$ (galaxies per Mpc^3; see Tully 1988), where different evolutionary mechanisms like interaction/accretion/merging may occur (Vollmer 2013, and references therein).

Table 2. Relevant characteristics of the ETGs. The morphological type, the average ellipticity, ϵ, the average central velocity dispersion, σ_c, and the maximum stellar velocity, V^*_{max}, are derived from HYPERCAT, http://leda.univ-lyon1.fr/. The average age, metallicity and [α/Fe] ratios (r_e/8 aperture) derived from optical spectra and modelling of Lick line-strength indices are taken from Annibali et al. (2007).

Ident.	Morphol. type	ϵ	σ_c (km s^{-1})	V^*_{max} (km s^{-1})	Age (Gyr)	Z	[α/Fe]
NGC 1209	-4.5 ± 1.0	0.58	240	211 ± 21	4.6 ± 0.9	0.051 ± 0.012	0.14 ± 0.02
NGC 1366	-2.3 ± 0.7	0.54	120	114 ± 19	5.9 ± 1.0	0.024 ± 0.004	0.08 ± 0.03
NGC 1415	0.5 ± 1.3	0.41	–	183 ± 10	–	–	
NGC 1426	-4.8 ± 0.5	0.32	162	114 ± 19	9.0 ± 2.5	0.024 ± 0.005	0.07 ± 0.05
NGC 1533	-2.5 ± 0.6	0.40	174 ± 9	–	11.9 ± 6.9	0.023 ± 0.020	0.21 ± 0.10
NGC 1543	-2.0 ± 0.8	0.23	143 ± 4	50±10	–	–	–
NGC 2685[a]	-1.0 ± 0.8	0.46	94	114 ± 14	–	–	–
NGC 2974[a]	-4.2 ± 1.2	0.38	220	225	13.9 ± 3.6	0.021 ± 0.005	0.23 ± 0.06
NGC 3818	-4.6 ± 0.8	0.37	191	91 ± 15	8.8 ± 1.2	0.024 ± 0.003	0.25 ± 0.03
NGC 3962	-4.8 ± 0.4	0.28	225	90	10.0 ± 1.2	0.024 ± 0.03	0.22 ± 0.03
NGC 7192	-3.9 ± 0.7	0.05	257	$\leq$20	5.7 ± 2.0	0.039 ± 0.015	0.09 ± 0.05
IC 2006	-4.2 ± 0.9	0.17	122	35 ± 35	8.1 ± 0.9	0.026 ± 0.004	0.12 ± 0.02

Notes. [a]Classified as FR = fast rotator by Emsellem et al. (2011).

2 THE SAMPLE

The galaxies in this work have been mostly selected from a larger sample of ETGs with MIR *Spitzer*-IRS spectra (see Rampazzo et al. 2013) and/or FUV *GALEX* images, which identify different degrees of activity in the nuclear region up to galaxy-scale SF, as we detail below. Many galaxies in the original sample have been observed previously in X-rays, and the data of the best studied, with the most information in the X-ray band, have been presented in Boroson et al. (2011), although with a different aim. We have chosen those located in low-density environments that lack X-ray data, and asked for X-ray observations with current satellites. We report here the results of our *Swift* campaign, adding an unpublished observation with *XMM–Newton* for NGC 1209. In the discussion we will add the galaxies in the Boroson et al. (2011) list that have an MIR classification. The X-ray nuclear properties of galaxies previously observed have already been presented in Rampazzo et al. (2013), in the context of MIR data.

MIR *Spitzer*-IRS spectra have been used to classify galaxies in five classes of 'activity', interpreted as different snapshots of an evolutionary cycle (see, e.g. Panuzzo et al. 2011; Rampazzo et al. 2013, and references therein). In this work we concentrate on those phases characterized either by fading or already quenched SF/AGN activities (classes 0–2), which characterize the galaxies we have obtained data for with *Swift*. As shown in Table 1, the nuclei of the ETGs in this sample either show evidence of anomalous PAHs, fossil signatures of a past SF or AGN activity (class 2: NGC 1533, NGC 2685, NGC 2974 and NGC 3962), or are passively or nearly passively evolving (class 0: NGC 1426, NGC 3818; and class 1: NGC 1209, NGC 1366, NGC 7192, IC 2006, respectively). Both the optical classification (LINERs or IN galaxies, see Table 1), and the low radio emission at 1.4 GHz confirm a low level of nuclear activity. MIR spectra are not available for NGC 1415 and NGC 1543, but they both show large-scale UV features.

As shown in Tables 1 and 2, the *K*-band luminosities span $\geq$1 order of magnitude and central velocity dispersions a factor of $\sim$2–3. Two galaxies, NGC 2685 and NGC 2974, are indicated as fast rotators by Emsellem et al. (2011). Very slow stellar velocity rotations are measured in NGC 1543, NGC 7192 and IC 2006. Ages, metallicities and [α/Fe] enhancements of the stellar component are obtained from modelling the line-strength indices (Rampazzo et al. 2005; Annibali et al. 2006). Within the r_e/8 aperture, about 1/2–1/3 in size of the MIR aperture, galaxies span a luminosity-weighted age from relatively young $\sim$5 Gyr (NGC 1209) to old (NGC 1533 and NGC 2974), consistent with >10 Gyr.

Several objects show clear signature of morphological and kinematical peculiarities both in the inner regions and at large scales at different wavelengths, often indicated as signatures of interaction/accretion/merging episodes occurred to the galaxy.

The classification reported in Table 1 from the Revised Shapley-Ames Catalog of Bright Galaxies (RSA) has been questioned for most objects. Regardless of the original classification, many have been 'reclassified' as S0s (NGC 1209 and NGC 1426, Capaccioli, Piotto & Rampazzo 1988; NGC 2974, Jeong et al. 2009, Marino et al. 2011b; IC 2006 and NGC 1415 in RC3, see also Laurikainen et al. 2011), or have a clear disc component in the luminosity profile (NGC 3818, Scorza et al. 1998). In addition, several objects show kinematical signatures of recent accretion/interaction events, like counter-rotating cores (e.g. NGC 2685, Ulrich 1975, Schechter & Gunn 1978; IC 2006, Schweizer, van Gorkom & Seitzer 1989) and decoupled components (e.g. NGC 1366, Morelli et al. 2008), sometimes in objects like NGC 7192 (Carollo & Danziger 1994), with a quiescent nucleus and little evidence of large-scale UV features.

Neutral or ionized hydrogen is also detected in many of them. Hα emission around the nucleus of NGC 1415 (Garcìa-Barreto & Moreno 2000, and reference therein) is offset from the nucleus and located just beyond the two extremes of the small, central stellar bar. NGC 2974 reveals the presence of an inner ionized Hα disc misaligned with respect to the stellar isophotes (by $\approx 20^\circ$; Ulrich-Demoulin, Butcher & Boksenberg 1984; Goudfrooij 1994; Pizzella et al. 1997), and an outer H I disc (Kim 1989) with the same rotation axis and velocity as the inner ionized one. Ryan-Weber, Webster & Bekki (2003) report an H I arc around NGC 1533 at 12–70 kpc radius, outside the FUV ring (see also Ryan-Weber et al. 2003; Werk 2010 for the H I distribution) with a mass of 7×10^9 M$_\odot$. An H I ring is also detected in IC 2006 at 6.5r_e (Franx, van Gorkom & de Zeew 1994), outside the optical galaxy, and NGC 2685 shows polar rings and polar dust-lanes (Józsa et al. 2009). A total of $\sim 10^9$ M$_\odot$ of neutral hydrogen is measured in NGC 1543 (Kilborn et al. 2005).

Table 3. Log of the X-ray and optical–UV observations.

Name	Satellite/ Instrument	Obs ID/ Filter	Date last obs	Exp. time[1] (s)
NGC 1209	*XMM–Newton* EPIC	0671700101	2012-02-13	64 872/72 845/72 882
NGC 1366	*Swift* XRT	00049396	2012-12-31	40 461.4
	Swift UVOT	*V*/*B*/*U*	2012-12-30/2012-12-30/2012-12-31	1112.2/1112.3/8627.5
		UVW1/*UVM2*/*UVW2*	2012-12-30/2012-12-30/2012-12-30	3595.7/11 825.6/13 483.7
NGC 1415	*Swift* XRT	00082265	2014-01-14	84 843.5
	Swift UVOT	*V*/*B*/*U*	2014-01-14/2014-01-14/2014-01-14	1562.5/1606.8/14 857
		UVW1/*UVM2*/*UVW2*	2014-01-14/2014-01-14/2014-01-14	22 887/18 595/23 990
NGC 1426	*Swift* XRT	00048113	2012-03-29	34 782.8
	Swift UVOT	*V*/*B*/*U*	2012-03-29/2012-03-29/2012-03-29	543.9/543.8/5765.2
		UVW1/*UVM2*/*UVW2*	2012-03-29/2012-03-29/2012-03-29	11 179.0/5744.4/9924.4
NGC 1533	*Swift* XRT	00049398	2012-12-24	37 396.8
	Swift UVOT	*V*/*B*/*U*	2012-12-24/2012-12-24/2012-12-24	1848.6/1848.5/ 13 198.2
		UVW1/*UVM2*/*UVW2*	2012-12-24/2012-12-24/2012-12-24	5607.6/7220.5/7412.4
NGC 1543	*Swift* XRT	00082264	2014-01-20	86 811.6
	Swift UVOT	*V*/*B*/*U*	2014-01-20/2014-01-20/2014-01-20	1575/1922/15 133
		UVW1/*UVM2*/*UVW2*	2014-01-20/2014-01-20/2014-01-20	20 155/29 743/17 414
NGC 2685	*Swift* XRT	00037812/00049762	2013-03-26 2	23 639.3
	Swift UVOT	*V*/*B*/*U*	2011-08-22/2011-08-22/2011-08-22	782.8/782.8/ 782.6
		UVW1/*UVM2*/*UVW2*	2013-03-26/2013-03-26/2013-03-26	6456.0/6517.4/7838.0
NGC 2974	*Swift* XRT	0004811	2012-07-02	37 122.4
	Swift UVOT	*V*/*B*/*U*	2012-06-29/2012-06-29/2012-06-30	1082.2/1082.2/7689.1
		UVW1/*UVM2*/*UVW2*	2012-06-29/2012-07-02/2012-07-01	3548.5/6709.5/16 495.0
NGC 3818	*Swift* XRT	00048112	2012-07-28	38 827.1
	Swift UVOT	*V*/*B*/*U*	2012-07-26/2012-07-27/2012-07-28	233.5/424.0/ 15 391.9
		UVW1/*UVM2*/*UVW2*	2012-07-27/2012-07-26/2012-07-27	3295.6/8497.2/10 616.5
NGC 3962	*Swift* XRT	00048114	2012-08-01	38 751.6
	Swift UVOT	*V*/*B*/*U*	2012-08-01/2012-08-01/2012-08-01	791.7/808.0/6699.1
		UVW1/*UVM2*/*UVW2*	2012-08-01/2012-08-01/2012-08-01	10 490.5/11 332.6/8487.1
NGC 7192	*Swift* XRT	00048111	2012-06-25	39 851.8
	Swift UVOT	*V*/*B*/*U*	2012-06-24/2012-06-24/2012-06-24	986.8/986.9/6786.6
		UVW1/*UVM2*/*UVW2*	2012-06-25/2012-06-24/2012-06-24	6163.2/15312.9/6926.8
IC 2006	*Swift* XRT	00049397	2012-12-28	37 894.9
	Swift UVOT	*V*/*B*/*U*	2012-12-28/2012-12-28/2012-12-28	1337.7/1430.7/11 180.9
		UVW1/*UVM2*/*UVW2*	2012-12-28/2012-12-27/2012-12-28	4991.9/6238.5/12 014.1

[1]For *XMM–Newton*, times are for EPIC pn-*M*1-*M*2 respectively; for UVOT, times refer to the filters specified in the corresponding column.

The presence of peculiar morphological structures as rings/arms or polar rings in basically half of the sample corroborates the hypothesis of the occurrence of past and/or ongoing interaction/accretion episodes.

3 DATA ANALYSIS

We obtained data from *XMM–Newton* (Jansen et al. 2001; Strüder et al. 2001; Turner et al. 2001) for NGC 1209, and *Swift* XRT and UVOT (Citterio et al. 1994; Gehrels et al. 2004; Burrows et al. 2005) for the other objects, as detailed in Table 3. NGC 2685 was also observed by *XMM–Newton* (PI Di Cocco) for ∼9000–14 000 s, however the observation is heavily contaminated by high background, and therefore will not be considered further.

The *XMM–Newton* data were analysed with the XMM-SAS version *xmmsas*_20131209_1901 software: they were first cleaned from high background flares and calibrated with the most current calibration files and threads available at http://xmm.esac.esa.int/sas. The resulting net observing times are reported in Table 3.

The *Swift*-XRT data of each galaxy were combined and a single event file and exposure maps were created, with the standard software (HEADAS software, v6.11.1, CALDB version 20120209) following the procedures described in http://heasarc.nasa.gov/docs/swift/analysis/ documentation.

Similarly, *Swift*-UVOT data observed in the same filter were combined for each galaxy. The final data set therefore contains *V*, *B*, *U*, *W*1, *M*2, *W*2 images for each of the galaxies observed with *Swift*, as we discuss below. The final exposure times per image are different, since they depend on the observing strategy that was used, namely to observe as much as possible in the filter-of-the-day in order to preserve the lifetime of the filter wheel.

We ran a detect algorithm to identify individual sources in the field. We used the *edetect_chain* task in XMM-SAS, in the central standard energy bands 0.5–2.0, 2.0–4.5 and 0.5–4.5 keV in EPIC-*M*1, EPIC-*M*2 and EPIC-pn, for NGC 1209. The algorithm finds a few sources within the D_{25} of the galaxy, one identified with the galaxy itself and several along the EW and S directions, following the emission shown in Fig 1. Most of them appear to be fluctuations of the extended emission, and are therefore not considered further.

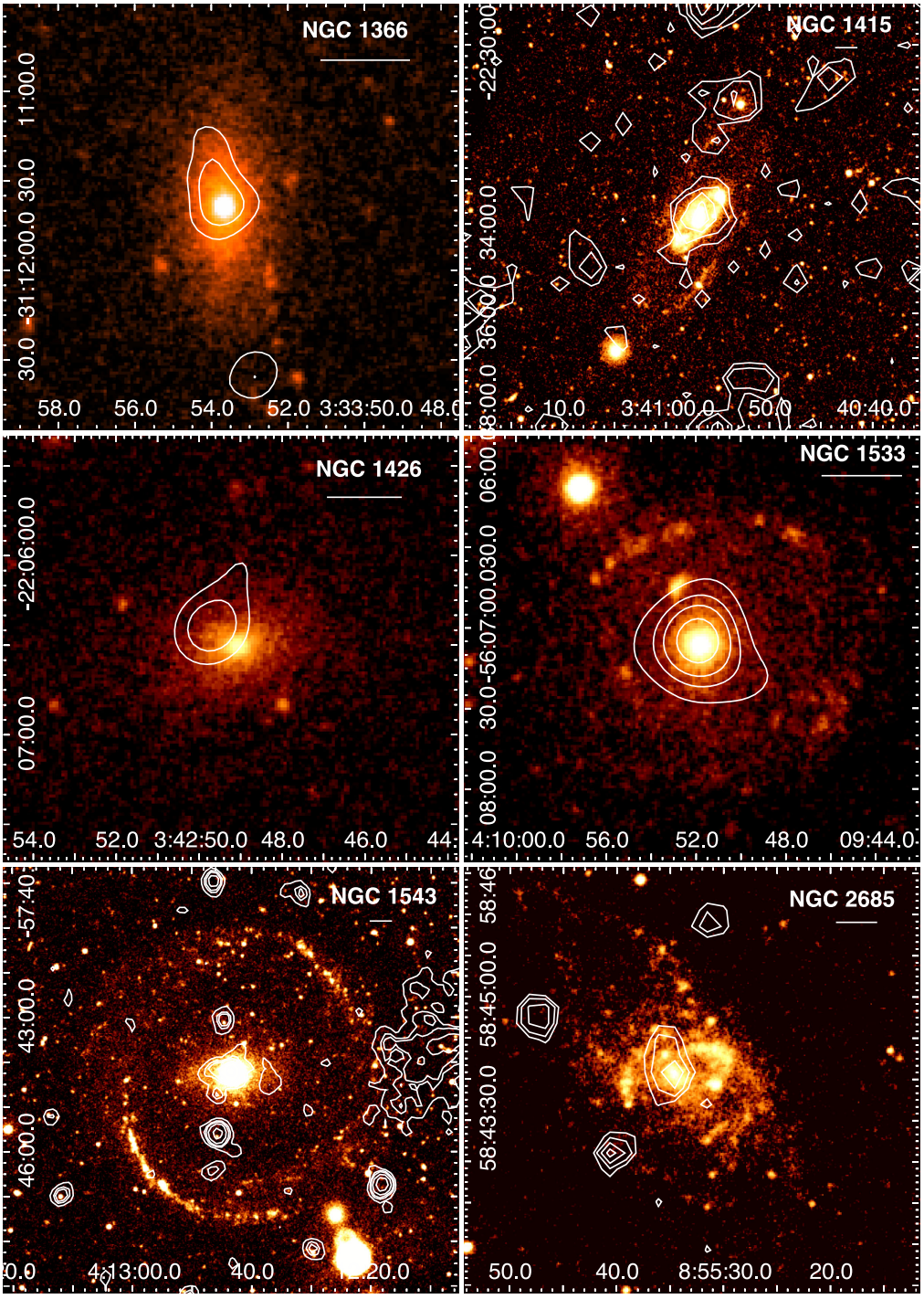

Figure 1. UVOT *M2* images of all X-ray-detected galaxies, with the contours from the smoothed image in the 0.3–4.5 keV band. A bar corresponding to 30 arcsec is plotted in each panel, to ease the comparison between the different scales of the images shown. For NGC 1209, we used the DSS image with the contours from the combined EPIC-pn+MOS image in the 0.3–4.5 keV band (white outer contours) and 2–4.5 keV band (inner blue contours).

The remaining five sources are listed in Table 4, together with an estimate of their net counts above the local background (the emission from the galaxy) and their luminosities. Source no. 4 has enough net counts in the EPIC-pn and can be identified in the central galaxy emission, so we extracted the spectrum and used the results to estimate the fluxes of all sources (see Section 6). One source (1) is at the northern boundary of D_{25} and has no optical counterpart, source 5 coincides with an optical source visible in the *V*-band image, the others are well within the optical body of the galaxy, embedded in the extended emission detected.

A similar procedure was followed for the galaxies observed with *Swift*-XRT: a detection algorithm was applied to full-size images in a single energy band of 0.5–3.0 keV. The source detected at the centre of the galaxy and those outside the D_{25} will not be considered further. In three cases, NGC 1543, NGC 2685 and NGC 3962, the algorithm detects sources in the galaxy, in particular 5, 2 and 1

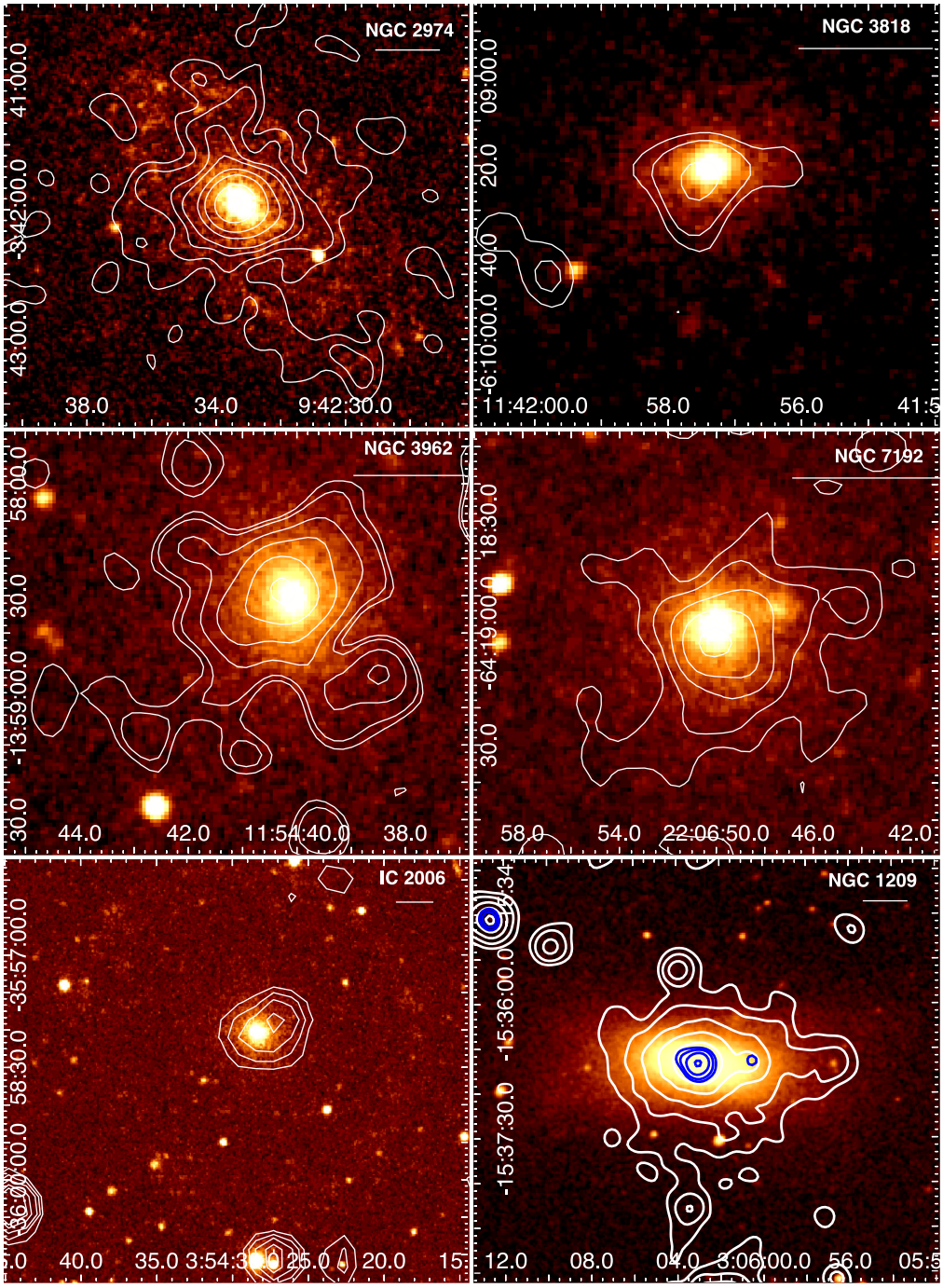

Figure 1 *– continued*

Table 4. Sources detected within the D_{25} in NGC 1209. Fluxes are estimated using a power-law model, rescaled from the results of source 4 based on the EPIC-pn data (see Table 6).

Src.	RA	Dec.	Radius	Counts and errors			Flux	Luminosity
			(arcsec)	EPIC-pn	EPIC-*M*1	EPIC-*M*2	(0.5–10 keV)	
1	3:06:03.912	−15:35:37.32	15	66 ± 12	17 ± 7	31 ± 8	3.1×10^{-15}	3.7×10^{38}
2	3:06:04.440	−15:36:30.60	12	281 ± 18	91 ± 10	89 ± 10	1.3×10^{-14}	1.6×10^{39}
3	3:06:04.728	−15:36:46.80	12	157 ± 14	46 ± 8	35 ± 7	7.3×10^{-15}	8.8×10^{38}
4	3:06:00.576	−15:36:39.49	15	268 ± 19	87 ± 11	59 ± 9	1.1×10^{-14}	1.5×10^{39}
5	3:05:56.736	−15:36:40.92	15	69 ± 12	10 ± 6	18 ± 7	3.2×10^{-15}	3.9×10^{38}

Table 5. Sources detected in NGC 1415, NGC 1543, NGC 2685 and NGC 3962 with *Swift*-XRT. Fluxes are estimated using a power-law model, rescaled from the results of the integrated emission from the whole galaxy (see Table 6).

Src.	RA	Decl.	Radius (arcsec)	Counts	Flux (0.5–10 keV)	Luminosity
NGC 1415						
1	3:40:52.8	−22:31:15.00	15	62 ± 8	2.3×10^{-14}	(1.5×10^{39})
2	3:40:55.6	−22:31:59.60	15	30 ± 6	1.1×10^{-14}	6.9×10^{38}
NGC 1543						
1	4:12:44.5	−57:43:02.20	15	25 ± 5	1.9×10^{-14}	9.0×10^{38}
2	4:12:36.9	−57:44:29.60	15	20 ± 5	1.5×10^{-14}	7.1×10^{38}
3	4:12:45.7	−57:44:42.20	15	17 ± 5	1.3×10^{-14}	6.2×10^{38}
4	4:12:45.6	−57:45:34.40	15	80 ± 9	6.1×10^{-14}	2.9×10^{38}
5	4:12:46.2	−57:46:23.60	15	19 ± 5	1.4×10^{-14}	6.7×10^{38}
NGC 2685						
1	8:55:47.3	+58:44:46.20	15	14 ± 4	3.6×10^{-14}	1.1×10^{39}
2	8:55:40.0	+58:43:07.50	15	14 ± 4	3.6×10^{-14}	1.1×10^{39}
NGC 3962						
1	11:54:35.9	−13:58:05.90	15	22 ± 5	3.4×10^{-14}	5.2×10^{39}

sources respectively, besides the central source (see Table 5). Two of the sources in NGC 1543 are aligned well with the galaxy, and two sources appear to coincide with a (background) optical source. The sources detected in NGC 2685 and NGC 3962 are at the edge of the optical extension of the galaxy and of the extended emission detected. A blue-UV background (?) source is visible at the position of the source in NGC 3962. We also report two sources for NGC 1415. They are both outside D_{25} but appear to be on the northern arm, with source 1 coincident with the bright star at the northern tip of the arm.

The luminosities of the detected sources, assuming all are in their respective galaxy, are consistent with the high-end tail of the luminosities of individual binaries, up to the Ultra Luminous X-ray Source (ULX) regime. While this is not implausible, a better spatial resolution is needed to accurately measure the luminosities of individual sources embedded in the large-scale galactic emission and better evaluate their real association with the host galaxy.

3.1 Maps

In Fig. 1 the smoothed contours of the X-ray emission for each galaxy are shown together with the images from the *M*2 filter, obtained from the UVOT observations, for the galaxies observed with *Swift* (see later), and from the DSS for NGC 1209. NGC 3818, NGC 2685, NGC 1366 and NGC 1426 are barely detected, with $\sim 48 \pm 8, 36 \pm 7, 26 \pm 6$ and 13 ± 5 counts respectively, while NGC 1533 shows a relatively compact emission peaked on the nucleus. The other galaxies show evidence of a larger scale distribution of the emission.

3.2 Radial profiles of the X-ray emission

We have examined the radial distribution of the emission and parametrized it with a β-type model using *sherpa* (in the CIAO software, version 4.6; Freeman, Doe & Siemiginowska 2001). Figs 2 and 3 show the results in the 0.5–3.0 keV band for the galaxies observed with *Swift*-XRT. The raw surface brightness profiles shown in Fig. 2 have been derived assuming azimuthal symmetry, and the annuli are chosen relative to the detected counts, balancing the request of a sufficient number of separate regions with the available statistics. In NGC 1533, NGC 1543 and IC 2006 the outer regions labelled 'ring' are chosen to reproduce the area where such features are seen in the optical/UV bands (see later).

Fig. 3 shows the net profiles, derived assuming a local background in regions located just outside the galaxy, in the same field. These estimates coincide with the nominal value, plotted in Fig. 2, except for NGC 3962, NGC 7192 and IC 2006, where a small difference is found with the nominal value (see Fig. 2).

For NGC 1415, NGC 1543, NGC 3962, NGC 7192 and IC2006 the best-fitting parameters (see Fig. 3) are far from the values that characterize the *Swift* point response function (PRF; see Moretti et al. 2005), $R_0 = 6$ arcsec and $\beta = 0.6$. NGC 3818 has very few counts, and the best fit would artificially require a core radius $\sim$2 arcsec, well below the instrument resolution. To obtain a parametrization, we put a lower limit to R_c at the value for the PRF, which gives $\beta \sim 0.48$, smaller (at $>1\sigma$) than that of the PRF. NGC 1533 data are consistent with the *Swift* PRF within the errors, with a small excess at the position of the ring. The fit with a single β-type model for NGC 3962 is statistically acceptable ($\chi^2_\nu = 0.7$, 10 degrees of freedom), but leaves an excess in the centralmost bin. Addition of a point source at the centre does not improve the quality of the fit (in terms of χ^2) but could accommodate a central source with an amplitude of 0.14 counts arcsec^{-2}, and a larger β-type model.

NGC 2974 was observed with the *ROSAT*-HRI in 1997 for 28 ks. The data obtained from the archive are plotted together with *Swift* in Fig. 4. The two profiles are arbitrarily normalized. The comparison between the data and the *ROSAT*-HRI PRF indicates that the X-ray emission from NGC 2974 is extended even at the *ROSAT*-HRI resolution, although we cannot exclude a contribution from a truly compact central source.

We will therefore consider all galaxies as extended sources, with the exception of the main body of NGC 1533, where we detect a compact source (at the *Swift*-XRT resolution). From the profiles (Fig. 2), we define a maximum radius of 90 arcsec for NGC 2974, 80 arcsec for NGC 3818, NGC 3962 and IC2006, 70 arcsec for NGC 7192 and 50 arcsec for NGC 1415 and NGC 1543, for the detected emission. Rings, as determined from the UV images, are outside the X-ray emission, at $\sim$50–100 arcsec for NGC 1533, $\sim$180–220 arcsec for NGC 1543, and $\sim$95–140 arcsec for IC2006.

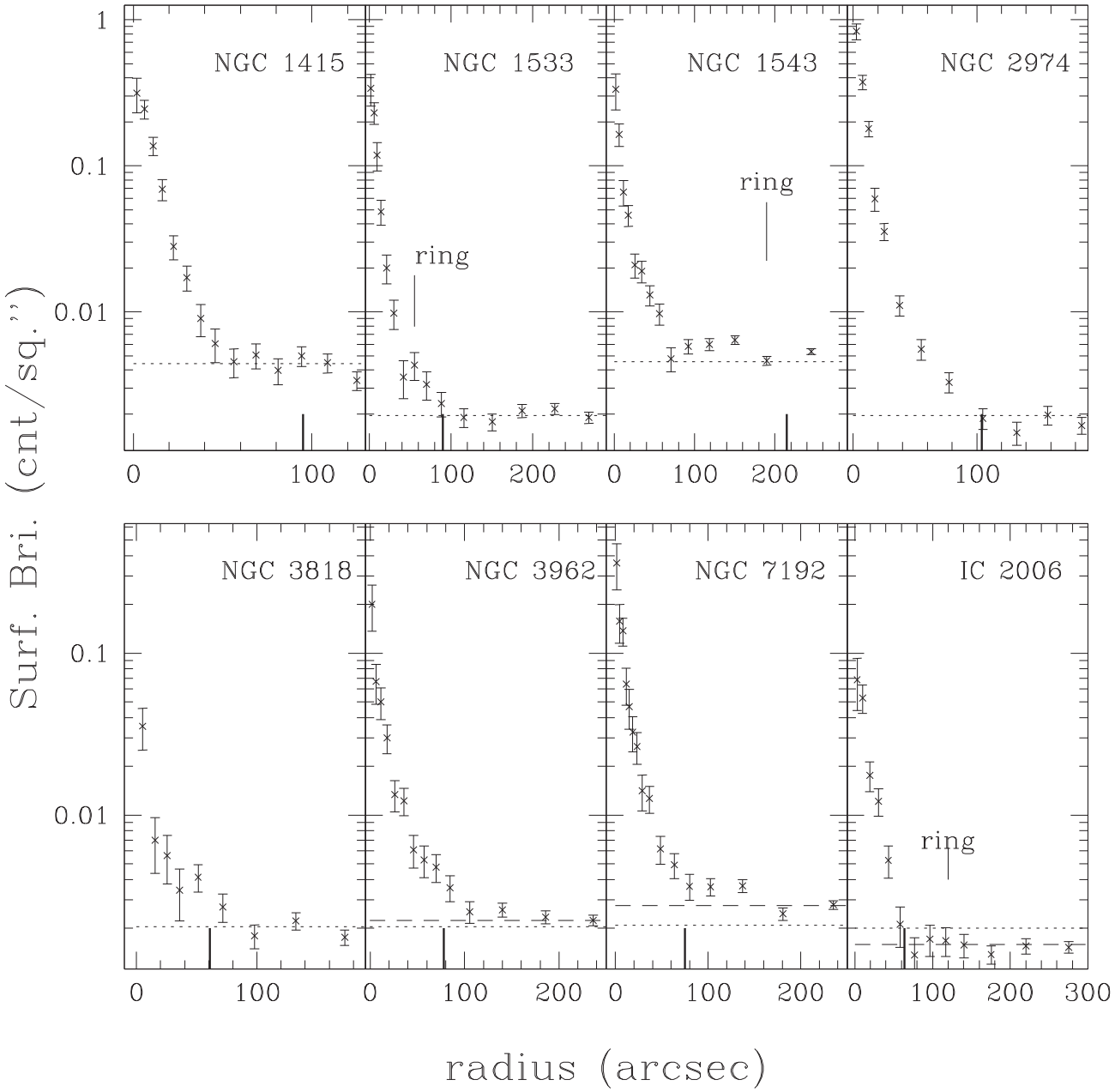

Figure 2. Raw radial profiles in the 0.5–3.0-keV energy band. The approximate position of the 'ring' features in NGC 1533, NGC 1543 and IC2006 are labelled. The horizontal dashed line indicates the background level (nominal value) for each observation. Minor adjustments (rescaling) have been done in NGC 3962, NGC 7192 and IC 2006, indicated by the dashed line. R_{25} (major axis, from the NASA/IPAC Extragalactic Database – NED) is indicated by the thick vertical line.

The EPIC-pn profile of NGC 1209 is shown in Fig. 5. The shape of the emission is clearly elongated in the ∼EW direction (cf. Fig. 1), similar to the optical light. We have used the stellar shape as a guide to define the elliptical annuli from which we derived the radial profile. We have used the 0.3–3.0 keV band, where most of the emission is. We have also identified the two orthogonal directions along the major and minor axes of the ellipse. The profiles obtained along the ∼NS and ∼EW directions and azimuthally averaged in the elliptical annuli are shown in Fig. 5. The emission has a different behaviour with galactocentric distance in the two directions, broader in the ∼EW direction. A comparison with the exposure map indicates a maximum extent of ∼200 arcsec. The azimuthally averaged net profile is given in Fig. 6.

3.3 Spectral results from the X-ray data

With the guide of the radial profiles, we extracted the spectral data from the circles with radii listed in Table 6, chosen to maximize the signal from each source. The slightly smaller radii include in all cases >90 per cent of the source counts, so total luminosities derived are virtually unaffected by this choice. No spectrum was extracted for NGC 3818, with only ∼50 net counts, nor for NGC 1366, NGC 1426 and NGC 2685, with even fewer counts. For NGC 1209, with significantly more counts, we extracted spectra from EPIC-pn from two different regions: an inner 30 arcsec circle and an outer ellipse, consistent with the shape and extension of the emission detected, plus the combined full area. We also extracted

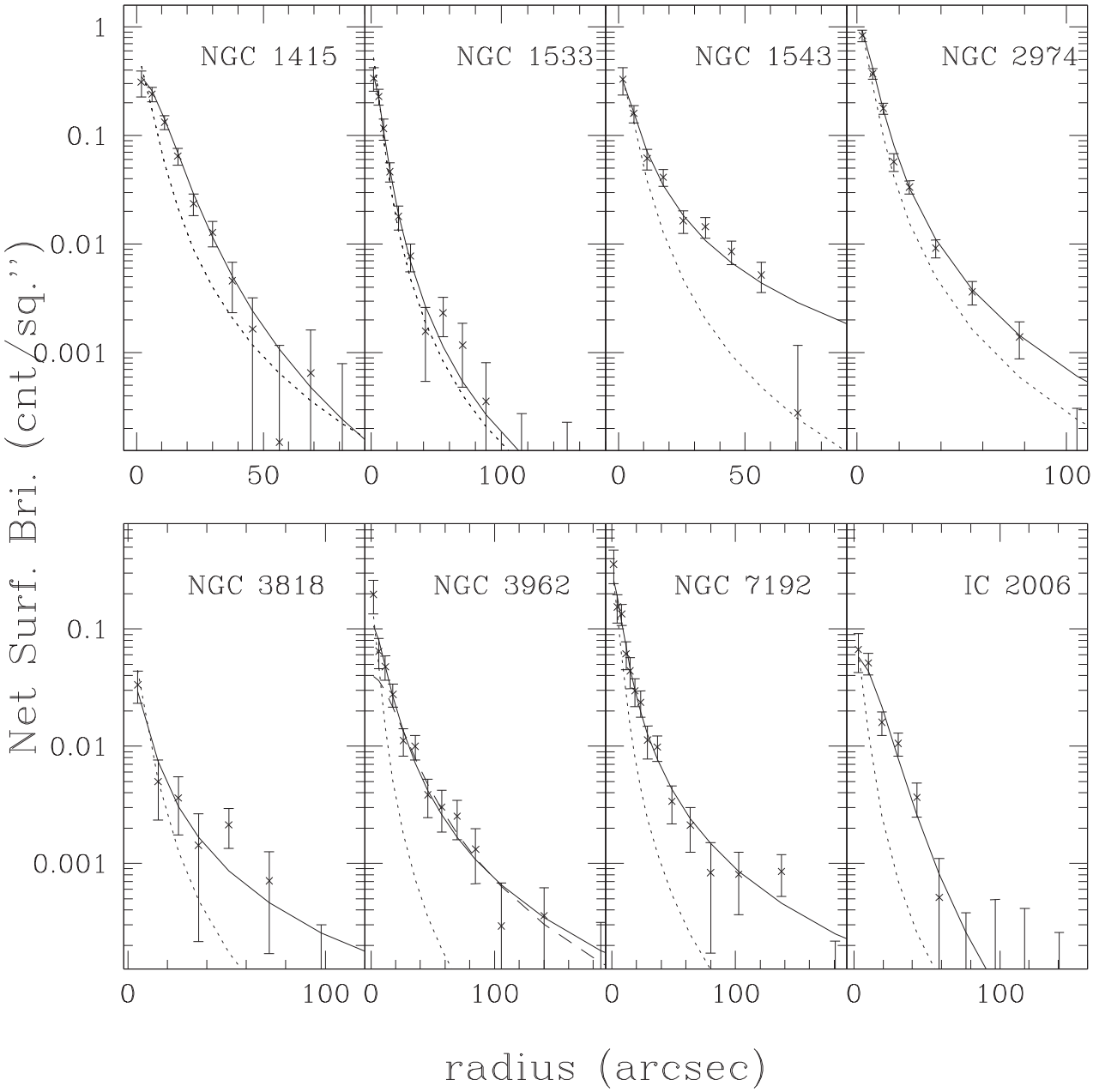

Figure 3. Radial profiles of the net emission in the 0.5–3.0-keV energy band. The continuous line represents the best-fitting β-model. NGC 1415: $r_0 = 15.1$ arcsec and $\beta = 0.88$; NGC 1533: $r_0 = 8.8$ arcsec and $\beta = 0.68$; NGC 1543: $r_0 = 5.3$ arcsec and $\beta = 0.48$; NGC 2974: $r_0 = 7.7$ arcsec and $\beta = 0.65$; NGC 3818: $r_0 = 6$ arcsec (fixed) and $\beta = 0.43$; NGC 3962: $r_0 = 11.5$ arcsec and $\beta = 0.55$ or $r_0 = 23.6$ arcsec and $\beta = 0.62$, with a lower normalization, to accommodate a central source (dashed line); NGC 7192: $r_0 = 7.4$ arcsec and $\beta = 0.53$; IC2006: $r_0 = 26.6$ arcsec and $\beta = 0.98$. The dotted line is the *Swift*-XRT response, parametrized as $r_0 = 6$ arcsec and $\beta = 0.66$.

the spectrum for source 4 in NGC 1209, as explained above, to estimate the fluxes and luminosities of the sources within the D_{25}. We have used a combination of a thermal plasma (model named APEC, with abundances fixed at 100 per cent solar from Grevesse & Sauval 1998; we note that we do not see significant changes in the spectral parameters derived with lower abundances) and power-law models to fit the data with XSPEC,[1] and we have included the AB+CV component (active stars and cataclysmic variables) estimated as in Boroson et al. (2011), normalized to the *K*-band luminosity of each object. In spite of the very limited statistics, many galaxies require a two-component spectrum. If the thermal component is not included in the model, we see a significant residual above the power-law continuum. In several cases the slope of the power law cannot be constrained and we have therefore fixed it at the value of $\Gamma = 1.9$ (the smallest value measured here, when the slope is a free parameter, see Table 6).

NGC 1533 and NGC 1543 can be fitted with a single power law, and the addition of the thermal component gives a negligible contribution. For NGC 1415, the thermal component is not required by the fit (adding it does not reduce the value of χ^2). Moreover, we find two relative minima, at 0.3 and 0.6 keV, with a power law $\Gamma \sim 2$–2.1.

[1] heasarc.nasa.gov/xanadu/xspec/

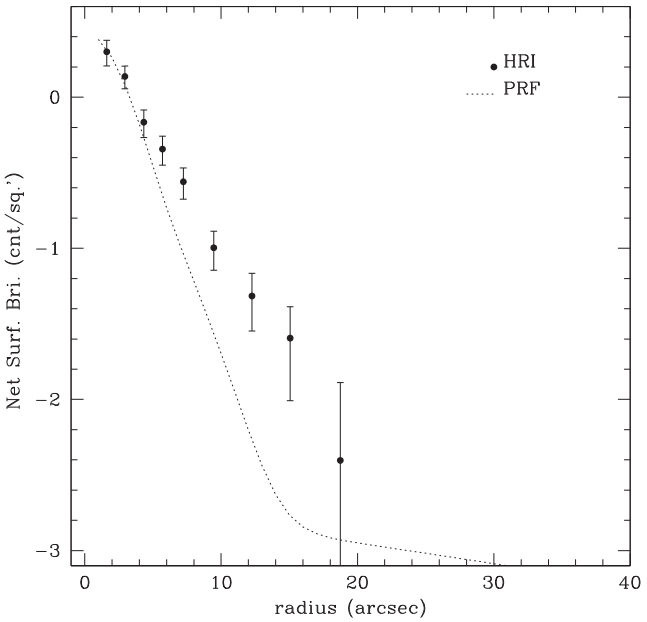

Figure 4. Inner region of the radial profiles for NGC 2974 from the *ROSAT* HRI data, compared to the HRI PRF (dotted line).

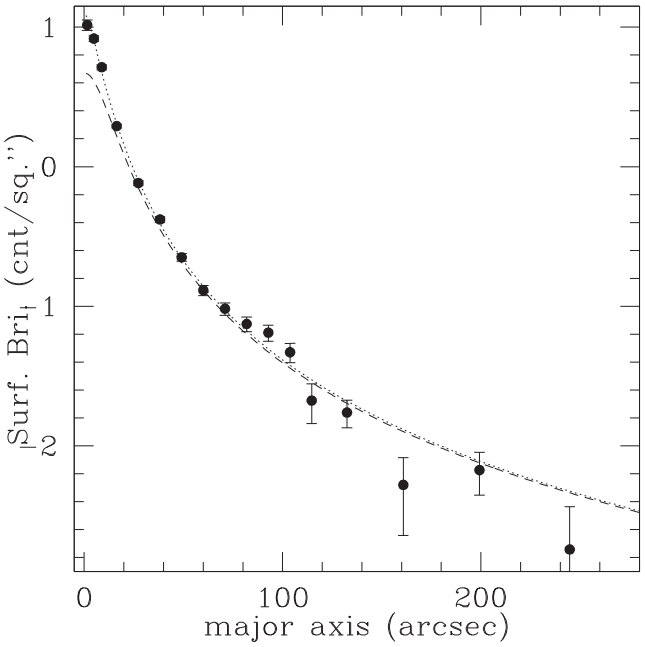

Figure 6. Net radial profile of NGC 1209. The profile can be parametrized (dotted line) by a combination of a β-type model, consistent with the point spread function of the EPIC-pn and a second model with $\beta = 0.57$ and $r_0 = 14$ arcsec (dashed line).

However, in either case, we find that the contribution from this component at the best-fitting value is not negligible ($L_x \sim 6$–10×10^{38}erg s^{-1}), therefore we list it as a component to the fit.

The total luminosities of the galaxies span from $L_x \sim 10^{39}$ erg s^{-1} to $\sim 2 \times 10^{40}$ erg s^{-1}. The thermal component, when present, contributes different amount in different galaxies: from $\leq$20 to $>$70 per cent of the total emission in the soft band. The lowest value for the gas component is measured in IC2006 at $L_x \sim 8 \times 10^{38}$ erg s^{-1}. The luminosities measured in the power-law components are consistent with what is expected from a population of low-mass binary sources (LMXB), estimated from the relation given in Boroson et al. (2011).

To estimate the luminosity of the galaxies with too few counts for a spectral analysis (NGC 1366, NGC 1426, NGC 2685, NGC 3818), we have rescaled the results for the single power-law fit (e.g. as in NGC 1533 and NGC 1543) to the detected total count rate. Similarly, we have estimated an upper limit to the 'thermal' component rescaling from the relative values estimated from NGC 1533

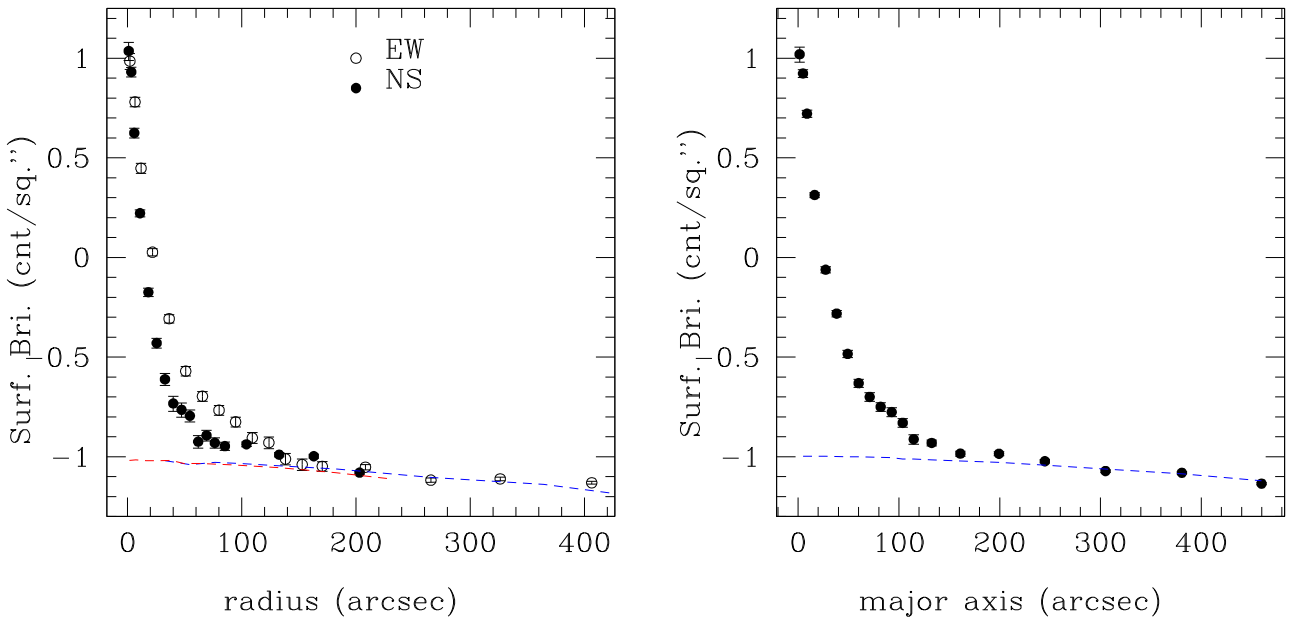

Figure 5. Radial profile of the EPIC-pn data of NGC 1209 in the 0.3–3.0 keV band. The profiles are obtained in concentric elliptical annuli, along the NS/EW direction (left) or azimuthally averaged (right). The dashed lines indicate the profile from the same regions applied to the exposure map and normalized to the data (red/blue for NS/EW, respectively).

Table 6. Spectral results.

Galaxy	Radius	Total counts	N_H	kT (90 per cent errors – 2 param.)	Γ	χ^2_ν (d.o.f.)	Flux/Lum (erg cm^{-2} s^{-1}/erg s^{-1}) 0.5–2.0 keV	Flux/Lum 2–10 kev
NGC 1209	72 arcsec / 145 arcsec	5896 ± 123	3.6×10^{20}	0.14 (0.1–0.23)	1.9 (1.5–2.5)	1.1 (177)	1.1×10^{-13}/1.5×10^{40}	5.2×10^{-14}/8.0×10^{39}
				0.61 (0.56–0.66)			1.3×10^{-14}[a]/2.0×10^{39}	
							6.1×10^{-14}[a]/9.4×10^{39}	
Centre	30 arcsec	3544 ± 65	4.2×10^{20}	0.61 (0.58–0.65)	2.0 (1.7–2.2)	1 (153)	6.5×10^{-14}/1.0×10^{40}	3.1×10^{-14}/5.4×10^{39}
							3.9×10^{-14}[a]/6.1×10^{39}	
Outer	72 arcsec / 145–30 arcsec	2088 ± 99	3.7×10^{20}[b]	0.31 (0.29–0.33)	1.9[b]	1.1 (76)	4.2×10^{-14}/6.5×10^{39}	2.3×10^{-14}/3.6×10^{39}
							2.4×10^{-14}[a]/3.8×10^{39}	
Source 4	15 arcsec	288.2 ± 20.7	3.7×10^{20}[b]	–	2.1 (1.9–2.4)	1.3 (32)	6.2×10^{-15}/8.5×10^{38}	5.7×10^{-15}/7.8×10^{38}
							–	
NGC 1415	45 arcsec	235 ± 17	9.0×10^{20}	0.3	2.1	1.3	6.2×10^{-14}/3.8×10^{39}	4.6×10^{-14}/2.9×10^{39}
			5.0×10^{20}	0.6	2.0	(13)	1.6×10^{-14}[a]/1×10^{39}	
NGC 1533	45 arcsec	147 ± 13	1.1×10^{20}[b]	–	1.99 (1.8–2.2)	0.9 (24)	5.7×10^{-14}/3.2×10^{39}	6.8×10^{-14}/3.8×10^{39}
							–	
NGC 1543	45 arcsec	222 ± 18	1.0×10^{21}	–	2.34 (1.8–3.1)	0 (25)	4.8×10^{-14}/2.3×10^{39}	3.4×10^{-14}/1.7×10^{39}
							–	
NGC 2974	52 arcsec	420 ± 21	7.4×10^{20}	1.22 (0.7–1.7)	1.9[b]	1.0 (24)	2.0×10^{-13}/1.1×10^{40}	2.2×10^{-13}/1.2×10^{40}
							3.4×10^{-14}[a]/1.9×10^{39}	
NGC 3962	75 arcsec[c]	248 ± 16	3.2×10^{20}[b]	0.29 (0.15–0.4)	1.9[b]	0.8 (20)	7.7×10^{-14}/1.0×10^{40}	6.9×10^{-14}/1.2×10^{40}
							2.2×10^{-14}[a]/3.3×10^{39}	
NGC 7192	63 arcsec	194 ± 17	2.5×10^{20}[b]	0.31 (0.25–0.45)	1.9[b]	1.3 (14)	9.2×10^{-14}/1.5×10^{40}	4.6×10^{-14}/7.9×10^{39}
							5.8×10^{-14}[a]/1.0×10^{40}	
IC 2006	60 arcsec	109 ± 14	1.1×10^{20}[b]	0.54 (0.25–0.85)	1.9[b]	0.8 (7)	5.2×10^{-14}/2.6×10^{39}	4.7×10^{-14}/2.3×10^{39}
							1.6×10^{-14}[a]/7.9×10^{38}	

Notes. Regions are all circles with the given radius, except for NGC 1209, where we use an ellipse (minor/major axis given). For outer region in NGC 1209 we mean the region outside the central 30 arcsec circle (centre).
[a]Thermal component only.
[b]Indicates that the parameter has been fixed at the given value.
[c]The source to the NW has been removed from the region.

Table 7. Summary of the X-ray luminosities used in the plots. The AB+CV component has been subtracted (based on L_K, Boroson et al. 2011, see Table 1), so we list the luminosities due to the LMXB and gas only, based on the results in Table 6.

Ident	log L_K $L_{K\odot}$	log L_x (Total) erg s^{-1} 0.5–10 keV	log L_x (LMXB) erg s^{-1} 0.3–8 keV	log L_x (gas) erg s^{-1} 0.5–2 keV
NGC 1209	11.09	40.40	39.86	40.04
NGC 1366	10.35	39.00	38.90	<38.48
NGC 1415	10.7	39.83	39.78	39.00
NGC 1426	10.6	38.95	38.85	<38.48
NGC 1533	10.91	39.85	39.87	<39.04
NGC 1543	10.93	39.60	39.69	<39.20
NGC 2685	10.37	39.20	39.11	<38.60
NGC 2974	11.48	40.36	40.28	39.28
NGC 3818	10.89	40.34	40.26	<39.74
NGC 3962	11.34	40.34	40.26	39.52
NGC 7192	11.06	40.36	40.12	40.00
IC 2006	10.53	39.69	39.60	38.90

and NGC 1543, both upper limits. We summarize the luminosities of the different components that we will use later in Table 7.

3.4 UVOT morphologies: a quick look

We have combined all UVOT observations of each galaxy in each of the filters we had requested: *V* (λ_c5468 Å), *B* (λ_c4392 Å), *U* (λ_c3465 Å), *W*1 (λ_c2600 Å), *M*2 (λ_c2246 Å) and *W*2 (λ_c1928 Å). The resulting images are shown in Fig. 7 (see Table 3 for details on the observations).

The depth of the images varies, since the observations were carried out in a hybrid configuration, that would ensure at least one observation in each of the six filters available, and longer observing times in the 'filter-of-the-day', to minimize turning the filter wheel that contributes to deteriorating it. Furthermore, it is well known that UVOT has severe photometric problems due to coincidence-loss for signals larger than 0.007 counts s^{-1} pixel^{-1} (see e.g. Hoversten et al. 2011, and references therein), which affect heavily the images taken in the *V* and *B* filters. Starting with the *U* filter, most of the image is unaffected, except for the nuclear region and areas of high surface brightness. We show all images in the complete set of six filters in this work, where we concentrate on a qualitative analysis of the morphological features characterizing each galaxy in the UVOT bands compared to the X-ray features. The quantitative analysis of the morphology and of the optical–UV spectral properties of these galaxies is left for a separate paper (Rampazzo et al., in preparation, hereafter Paper II).

NGC 1366, NGC 1426, NGC 3818, NGC 3962 and NGC 7192 show similar structures at all UVOT wavelengths. NGC 1366, the faintest galaxy in our sample (see *K*-band luminosities in Table 1), shows a compact, bright nucleus embedded in a disc seen nearly edge-on. A knot west of the nucleus of NGC 7192, otherwise a normal ETG, starts to appear in the *U* filter, and becomes relatively more prominent going towards *W*2. The nature the knot is unknown at the moment, but it is also visible in the *GALEX* image

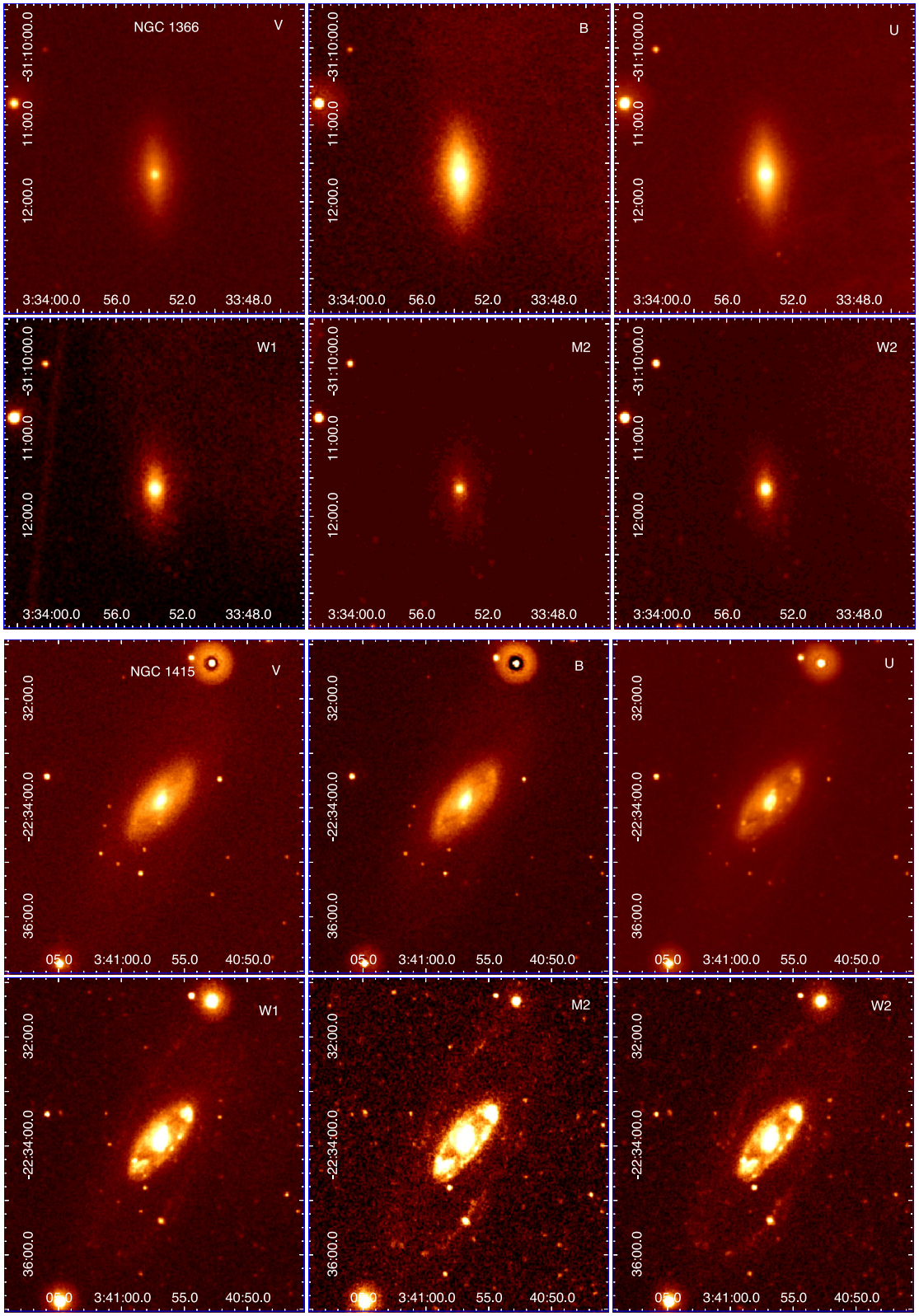

Figure 7. *Swift*-UVOT images of the ETGs in all filters used.

NGC 1533, NGC 1543 and IC2006 have well-defined almost circular rings that appear at *U*–near-UV (NUV) wavelengths. In NGC 1533, the nucleus, a bar and disc are clearly visible in the *V* and *B* bands. The ring/arm-like structure, already noticed by Werk (2010) and Marino et al. (2011a) at a radius of ∼45–55 arcsec, together with an inner feature ∼25 arcsec NNE of the nucleus, appears in the *U* band. The bar progressively disappears at shorter wavelengths, while the nucleus remains.

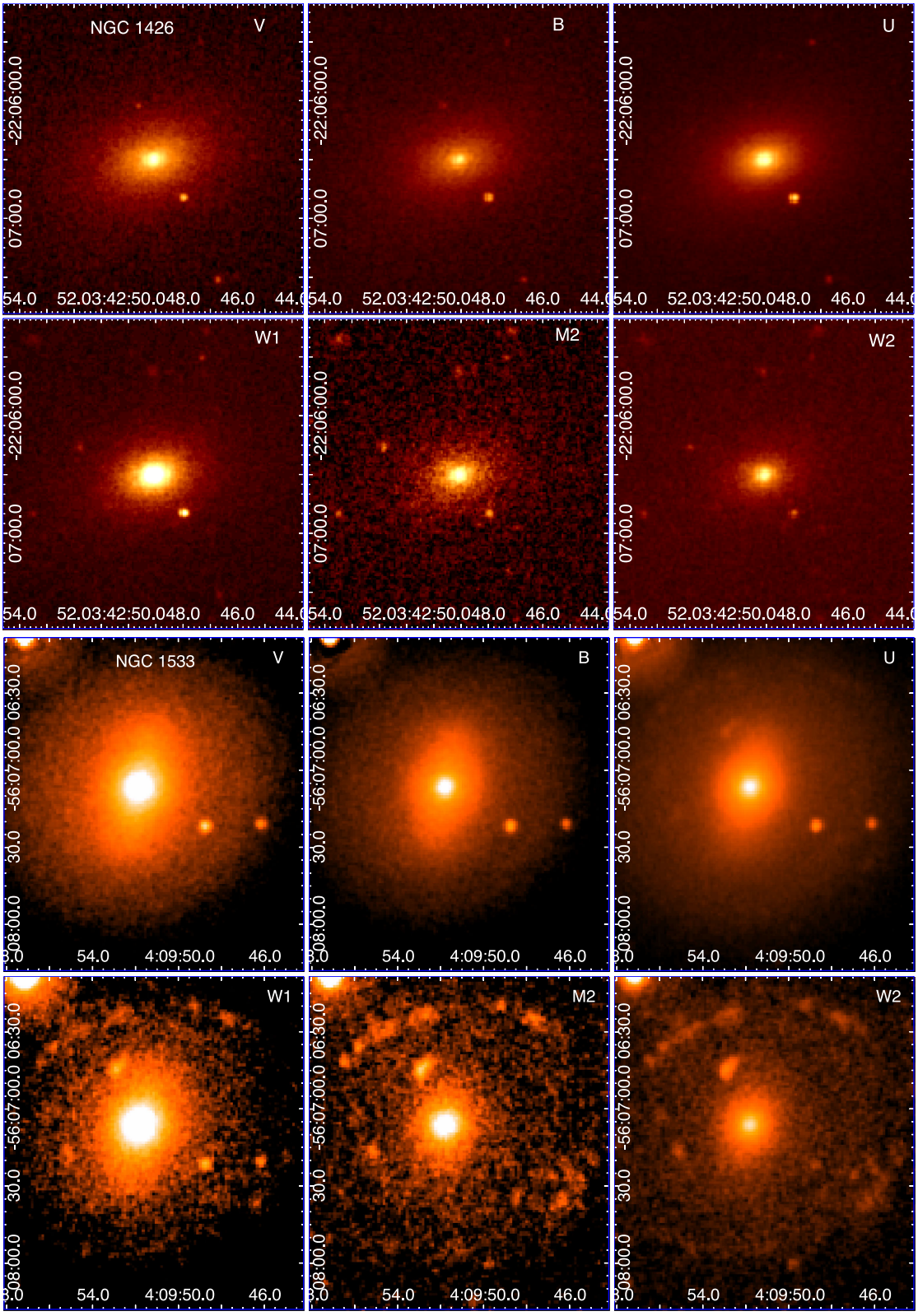

Figure 7 – *continued*

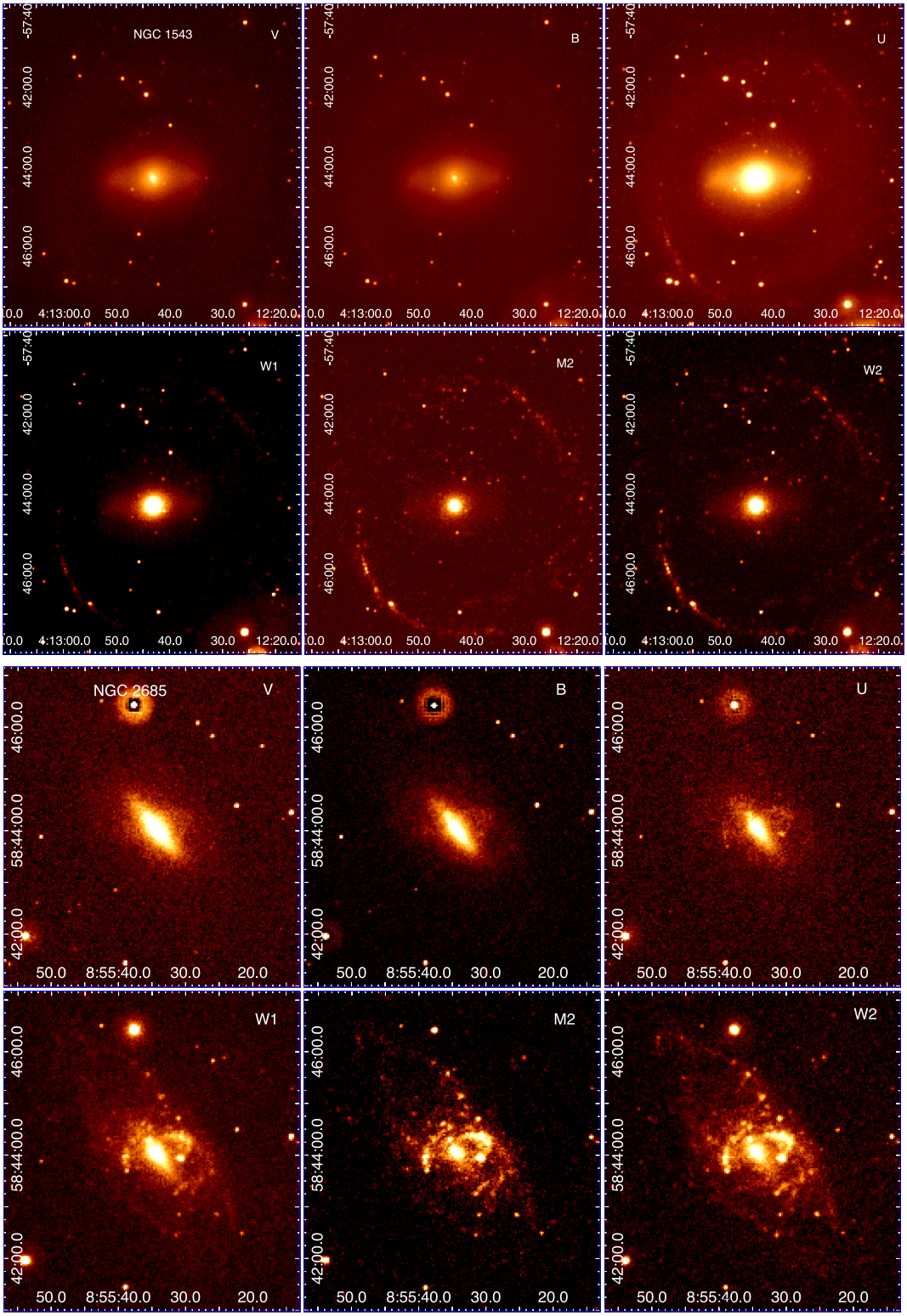

Figure 7 – *continued*

NGC 1543, seen nearly face-on, shows a double bar. The inner bar (≈23 arcsec in diameter) is oriented 30° NE while the outer bar, nearly aligned EW, has a diameter of about 2.3 arcmin in the *V*, *B* and *U* bands. Only the outer bar is still visible in the *W*2 band. The outer ring (about 6 arcmin in diameter), already detected in optical bands (see on-line catalogue by Ho et al. 2011), has a knotty and irregular appearance, reminiscent of an arm-like structure, likely star-forming regions at large galactocentric radii.

Starting from the *U* band, IC 2006 shows a well-defined almost circular ring/arm-like structure, with a knotty appearance in the *W*2 band, at an average distance of ∼130 arcsec. It corresponds to the H I ring found by Franx et al. (1994).

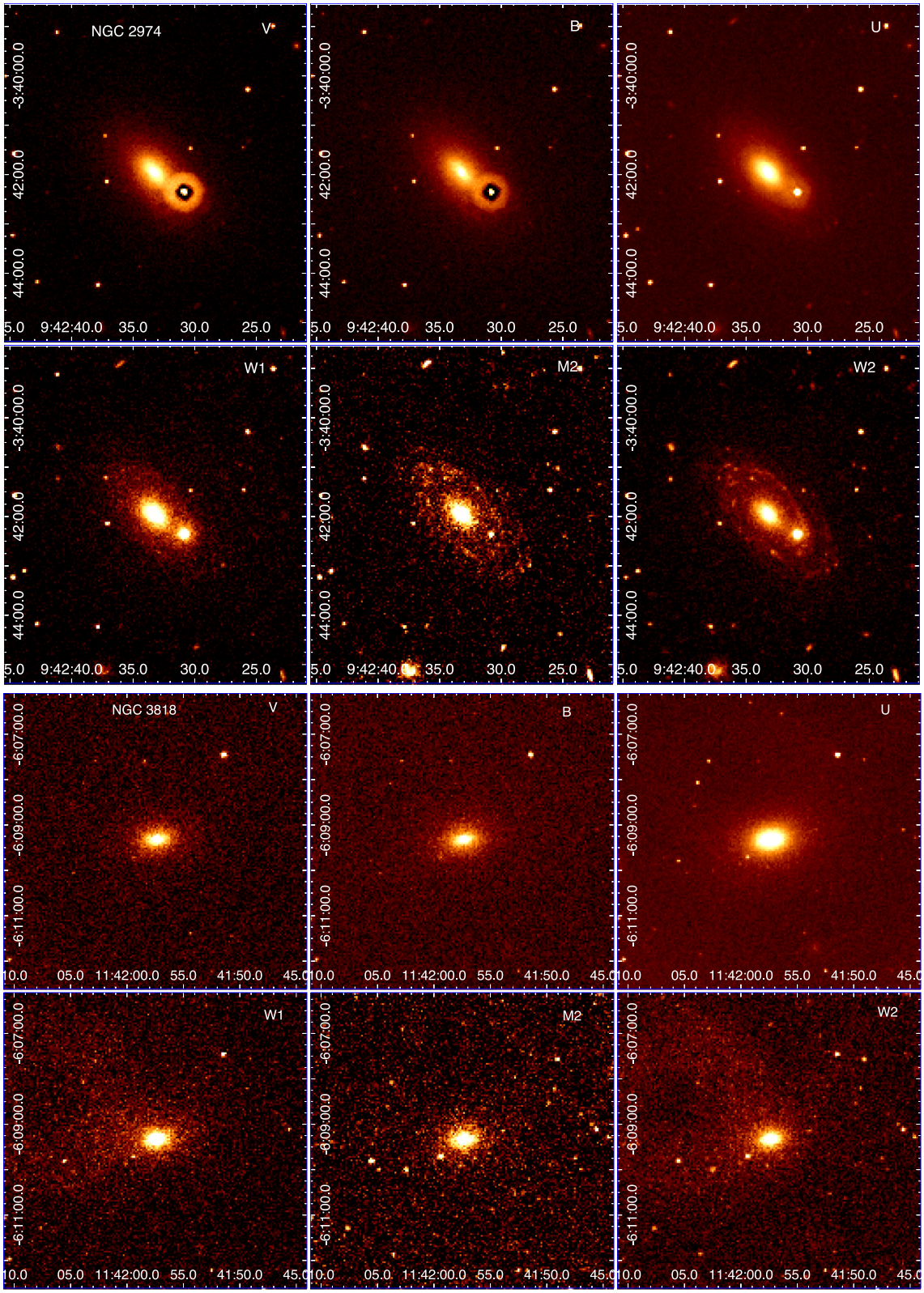

Figure 7 – *continued*

NGC 1415, NGC 2685 and NGC 2974 have more spectacular and complex features. NGC 1415 shows a bulge (a bar?) plus inner (about 1.5 arcmin diameter) smooth, disc-like structure crossed by a dust-lane. A ring structure appears at its edge and its intensity increases from the *U* band towards shorter wavelengths. The ring is knotty, with the brightest knots at NW and SE. An outer (about 5 arcmin diameter) faint ring/arm-like structure appears in the *U* band and becomes relatively sharper at shorter wavelengths.

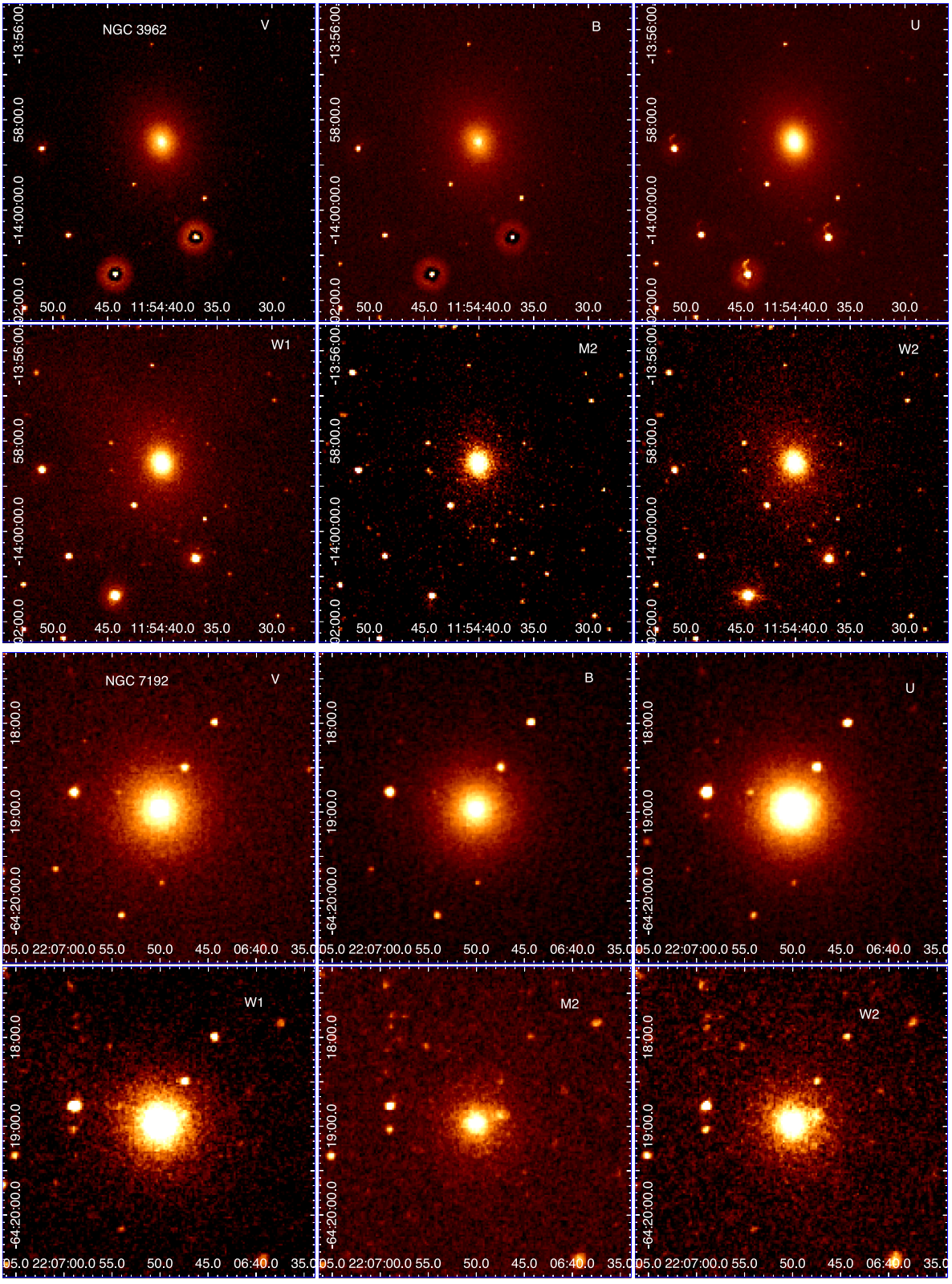

Figure 7 *– continued*

The *V*-band image of NGC 2685 shows a bright nucleus and a nearly-edge-on disc component, with a hint of a protuberance to the NNW, that becomes a bright ring at shorter wavelengths. An outer ring coincident with H I emission (detected by Gallagher, Faber & Balick 1975; Bieging 1978 and studied more recently by Józsa et al. 2009) emerges in the *W*1 band and becomes progressively more prominent at *W*2. Both the inner and the outer rings have a knotty structure suggesting the

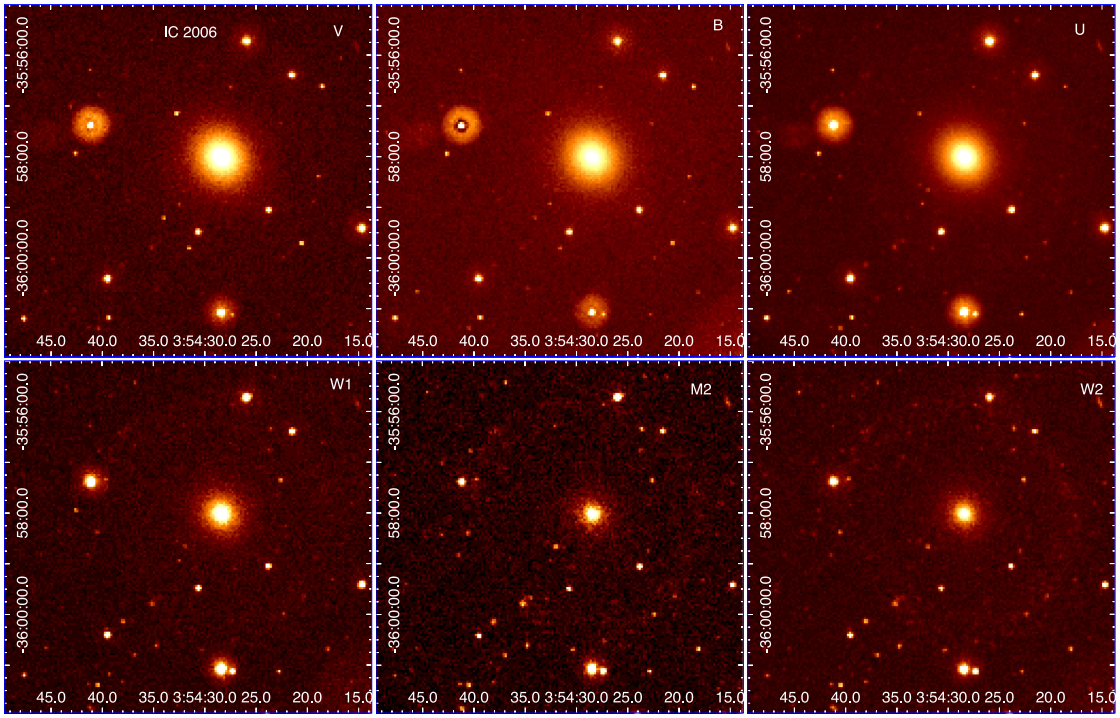

Figure 7 – *continued*

presence of star-forming regions at large distances from the galaxy centre.

The knotty, arm-like structure in the disc of NGC 2974 detected by Jeong et al. (2009) and Marino et al. (2011a) in FUV/NUV is clearly visible in the *M*2 and *W*2 images.

4 DISCUSSION

4.1 X-ray properties

All galaxies in the present sample have been detected, and half of them have a measurable component of X-ray emitting gas, with gas luminosities ranging from $L_{\rm x} < 10^{39}$ to $\sim 10^{40}$ erg s^{-1}.

Fig. 8 shows the distribution of the luminosities in the X-ray components (total, LMXB and hot gas) relative to L_K and σ of the stellar component. We have used the scaling relations derived in Boroson et al. (2011) to estimate the contributions from the unresolved low-luminosity stellar component of AB+CV linked to the *K*-band emission, in order to measure the 'pure' thermal and LMXB components. In most cases the AB+CV emission is well below the gas component detected, in particular if the AB only are considered, except for NGC 2974, where $L_{\rm x}(gas) \sim L_{\rm x}(AB + CV)$. As already noticed since the first *Einstein* data (Forman et al 1979; Trinchieri & Fabbiano 1985), the relation between X-ray and stellar properties for ETGs is complex. The roughly linear relation between L_X from the LMXB component and L_K from the stars discussed in the literature (White, Sarazin & Kulkarni 2002; Colbert et al. 2004; Kim & Fabbiano 2004; David et al. 2006; Boroson, Kim & Fabbiano 2011), is confirmed here (middle panel of Fig. 8, where the measured L_X scatters around the predicted values). We also confirm the large spread between L_X from hot gas and L_B, L_K or σ (rightmost panels). As a note of caution, we remark that the small statistics of our data does not allow us a precise determination of the hard component (in most cases the slope was fixed at a given value), nor of the possible contribution from an AGN (which we could not separate, if present, although it would be of very low luminosity). None the less the agreement between predicted and expected values is very good, and the lack of a hot ISM in some objects, though poorly measured, seems to be independent of their L_K or σ.

To enlarge the statistical validity of any suggestion we can make, based on the small sample, we have added the galaxies analysed by Boroson et al. (2011), who have used the best-available *Chandra* data for a sample of 30 ETGs not at the centre of clusters (although several belong to groups or are in the Virgo cluster). This represents to date the largest homogeneous set of X-ray results for ETGs, against which we can compare our results. About half of the Boroson galaxies have a MIR classification (Rampazzo et al. 2013), and only a few have features observed in the UV.

As can be clearly seen by the comparison shown in Fig. 9, our sample spans a smaller range of X-ray luminosities, which is a consequence of the fact that we have not included high-luminosity gas rich objects like NGC 4472, and we cannot determine with high accuracy gas luminosities well below the AB+CV component, as Boroson et al. (2011) could in ∼30 per cent of their objects. We sample better the low velocity dispersion range, and confirm a general trend that lower σ objects show a lower total $L_{\rm x}$. With the exception of NGC 2974, we measure a temperature of kT∼0.3 keV, and $L_{\rm x}(gas) \sim 1 \times 10^{39}$ erg s^{-1}, in line with Boroson's results. Therefore, although our new X-ray data have lower quality compared with those used by Boroson et al. (2011), our results are in agreement with theirs and we confirm the considerations already done by these authors.

4.2 X-ray properties, MIR classes and UVOT images

Understanding the mechanisms, inner secular or external, that drive galaxy evolution, and determining the time-scales, the effects and

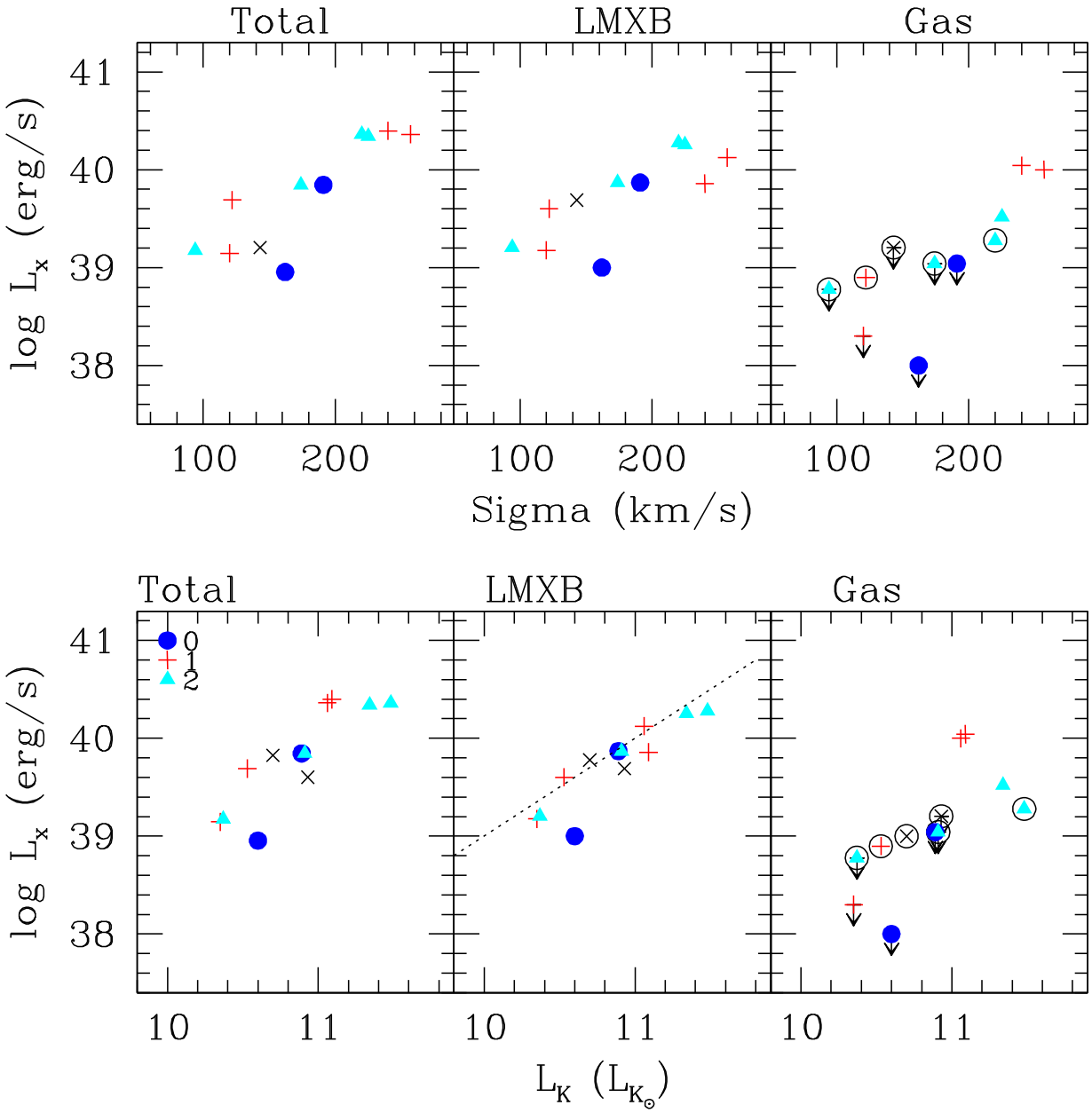

Figure 8. Total X-ray luminosity (0.5–10.0 keV band); X-ray luminosity of the power-law component (presumably due to LMXB, in the 0.3–8.0 keV band) and gas luminosity (0.5–2.0 keV band) plotted versus *K*-band luminosity (bottom panels) and σ (top panels). Different colours (shapes) identify different MIR classes, as indicated in the legend. Black crosses indicate undefined MIR class (NGC 1415 and NGC 1543), galaxies with UV structures are identified by the larger circles. The dotted line in the middle panel indicates the expected contribution from LMXB from Boroson et al. (2011).

the spatial extent of the episodes of activity (AGN, star formation) induced by these mechanisms, are among the main motivations for this study.

From a morphological point of view, the present sample is composed of two broad classes: about half of the ETGs have a regular, wavelength-independent appearance (NGC 1366, NGC 1426, NGC 3818, NGC 3962, NGC 7192; see Section 3.4). The other half show ring/arm-like structures (NGC 1415, NGC 1533, NGC 1543, NGC 2685, NGC 2974, IC 2006), preponderantly emerging in the UV wavelengths, i.e. in *W*2, *M*2 and *W*1 bands imaged with UVOT, most likely associated with episodes of recent SF activity. In addition NGC 7192 is a shell galaxy (Malin & Carter 1983) and displays a knot of emission at ∼15 arcsec west of the nucleus, which becomes evident only starting from the *W*1 image (see also NUV image from *GALEX* in Marino et al. 2011a).

NGC 1209 does not have *Swift* observations. Annibali et al. (2007) suggest a young luminosity-weighted age of ∼5 Gyr.

Ring/arm-like features are found out to several effective radii (see Paper II). Such features are connected with the presence of H I gas, often co-spatial with these features (see Mazzei et al. 2014a), suggesting a connection and fuelling of the recent or even ongoing SF.

The innermost regions of all but two galaxies (generally an area of 2–3 $r_e/8$) have been observed also with the *Spitzer* telescope and classified according to their spectral features in classes of increasing 'SF activity' (see Rampazzo et al. 2013, and Table 1). According

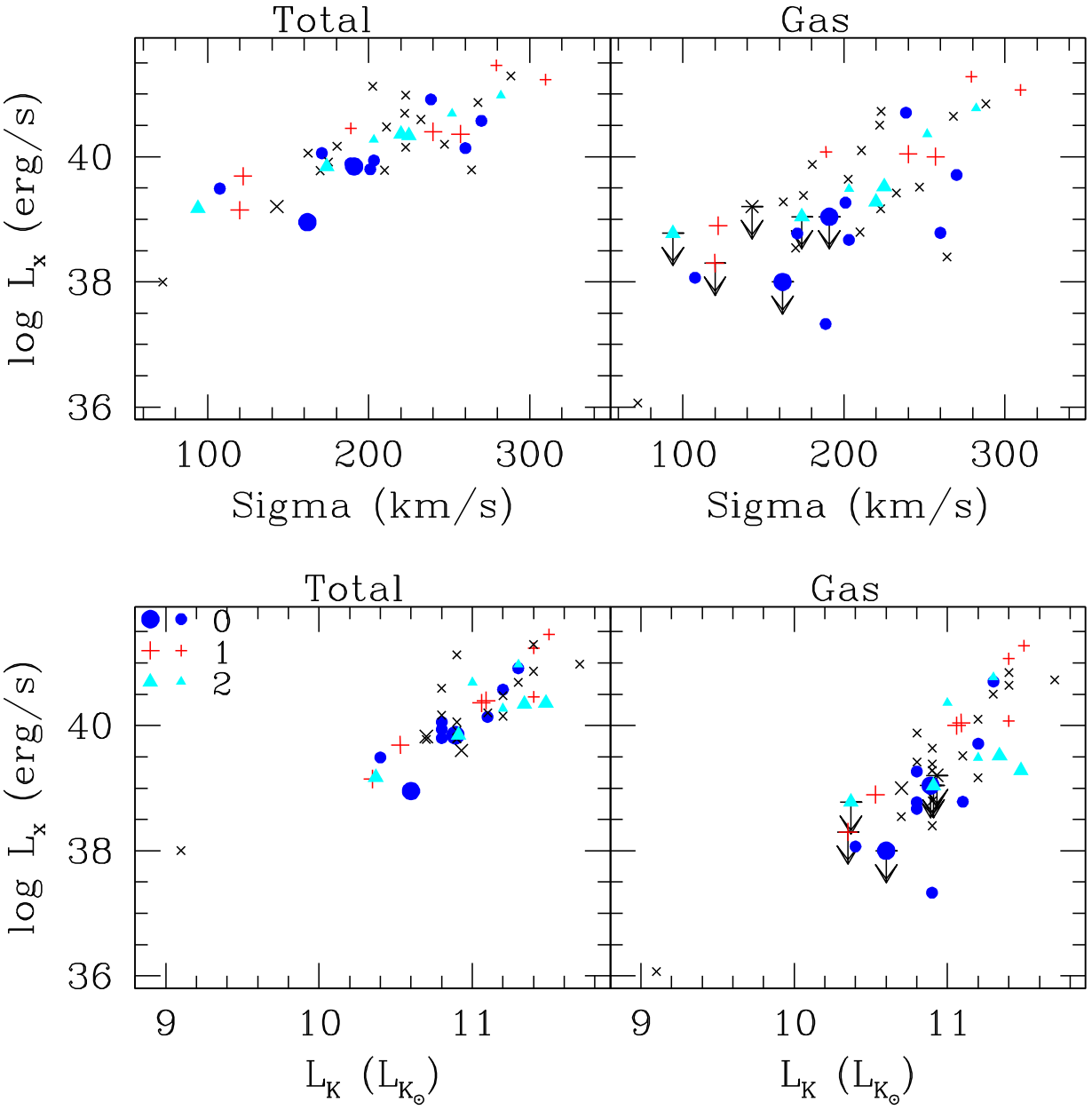

Figure 9. Total and gas X-ray luminosity plotted versus *K*-band luminosity (bottom panels) and σ (top panels) for the present sample (symbols as in Fig. 8) and for Boroson et al. (2011) sample (smaller sizes). Black crosses indicate MIR classes other than 0–2 (class 3: NGC 4697; class 4 NGC 1052, NGC 4261, and many undefined).

to their MIR classification, only NGC 1426 and NGC 3818 have a truly 'passive' spectrum. NGC 1533, NGC 2685, NGC 2974 and NGC 3962 belong to MIR class 2, i.e. they show H_2 emission lines, anomalous PAH interband ratios and nebular emission lines typical of LINERs, and suggestive of recent SF in their nuclear regions. NGC 1209, NGC 1366, NGC 7192 and IC 2006 are intermediate cases, passively evolving systems with only weak signatures of ionized gas in their nuclei (e.g the [Ne II] and [Ne III] lines) and no PAH features. The optical spectrum in the nuclear region suggests that emission lines in IC 2006 may be ionized by thermal emission (see Table 1). NGC 1533 and NGC 2972 are classified as LINERs while NGC 2685 may host a Seyfert nucleus, which is not bright at X-ray wavelengths.

Five galaxies do not show evident signatures of large-scale SF, which might be discovered in the more careful analysis planned (see Paper II, and *GALEX* images for NGC 1426 and NGC 3818, Marino et al. 2011a). However, only three of them, namely NGC 1366, NGC 1426, NGC 3818, are passively evolving, i.e. do not show emission either both in the optical and in the MIR (class 0/1), and have little evidence of 'other' signs of rejuvenation episodes.

The two brighter galaxies, NGC 3962 and NGC 7192, show emission lines in the nucleus and are LINERs in the optical. Moreover, NGC 3962 contains $\sim\times\ 10^9$ $M_\odot$ of H I (Serra & Oosterloo 2010), a mass more than four times larger than that revealed in NGC 2974 (5.8×10^8 $M_\odot$), which instead shows a complex large-scale structure of arcs and outer arms (see Fig. 7), but similar nuclear properties.

Based on this very small sample, observations suggest that the mechanism generating the large-scale SF may also induce different forms of activity, SF and/or AGN, in the galaxy nucleus, although

characterized by different time-scales. UV signatures are generally produced by young massive stars, so the average time-scale of this tracer is of the order of a few to several Myr. The MIR features are linked to dust from evolved carbon stars and SN remnants, so they could last longer than the young stars tracing the UV (see also Rampazzo et al. 2014).

The relation between MIR classes and nuclear X-ray properties have been investigated by Rampazzo et al. (2013). They find a weak relation between the PAH 11.3/7.7 μm ratio and the average value of the measured X-ray luminosity in the nucleus, in the sense that larger values of PAH ratios correspond to larger X-ray luminosities (analysis limited to MIR classes 2–4). However, there was no attempt to disentangle the contribution from an AGN component, which in fact could explain the difference in L_x in class 2 and 3 objects.

MIR classes and evidence of large-scale SF have been marked in the plots of Fig. 8, in an attempt to identify possible trends with the large-scale X-ray emission. We work on the hypothesis that there is no significant contribution from a nuclear source in the galaxies in the present sample. In spite of the reduced size of the sample, we notice that modest SF activity in the nuclear area does not seem to influence the total X-ray emission, nor the presence and amount of hot gas. While it is true that gas could not be detected in either of our 'passive' objects, there seems to be no obvious link between $L_x(gas)$ and nuclear activity: in fact two of the MIR = 1 galaxies have the largest gas luminosity and $L_x(gas)/L_K$ in this sample, well above MIR = 2 objects, and there seems to be little relation between hot gas and MIR classes. Similarly, signs of large-scale SF activity (identified by the big circles in Fig. 8) do not appear to be linked to the overall hot gas emission. The suggestion that emission is present at the location of the ring in NGC 1533 (see Fig. 2) might indicate that we should expect local effects (see, e.g, the results in the ring of NGC 1291, Luo et al. 2012), but the effect on the global emission is too small to be measured with these data.

The lack of relation between MIR classes and X-ray emission is confirmed by the plots in Fig. 9, where we include the Boroson et al. (2011) sample.

We performed a rapid inspection of all images available in the *GALEX* archive for the ETGs of the sample of Boroson et al. (2011). Unlike our sample, the vast majority of them have no FUV features, with three exceptions: NGC 1427 (in Fornax, MIR class 0, low gas luminosity) shows a FUV blue inner clump, possibly corresponding to the companion galaxy PGC 2793617. Temi, Brighenti & Mathews (2009) report a detection of dust in MIPS data, which could suggest that residual SF may be present. The other two galaxies, both MIR class 1, are members of the Virgo cluster and have the most luminous gas component in the sample: the inner region of NGC 4649 is slightly bluer (FUV) than the outer one, and NGC 4472 shows the presence of a blue tail towards the galaxy PGC 41258.

4.3 Hot gas and stellar age

SF, either detected through the UV emission or the MIR classes, should also be related to the age parameter, which has been used previously in relation to the emission from hot gas in ETGs (Memola et al 2009; Boroson et al. 2011).

A major limitation in determining ages in ETGs is intrinsic to the methods generally used, which rely on spectrophotometric population synthesis techniques based on nuclear optical data. The age–metallicity degeneracy, that propagates even small spectrophotometric errors into a huge age spread, comparable to a significant fraction of the age of the Universe (e.g. Worthey 1994), and the presence of even small amounts of relatively recent SF may cause a spread in the age from ∼1 Gyr to a Hubble time (e.g. Longhetti et al. 1999; Trager et al. 2000a,b; Annibali et al. 2007). The slit nature of the spectra also makes these estimates position-dependent, all of which might add to explaining the large spread in estimates found for several objects. A multiwavelength approach, based on a wealth of optical/IR/UV images and spectra applied to a sample of 65 ETGs in low-density environments was able to constrain the stellar age (Rampazzo et al. 2005; Annibali et al. 2006, 2007, 2010).

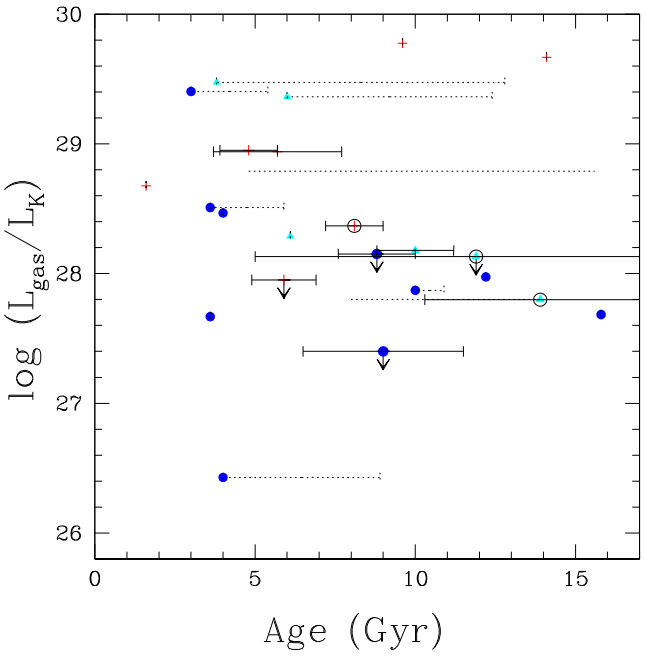

Figure 10. Gas X-ray luminosities measured from the L_{XGas}/L_K ratio plotted versus 'Age' for galaxies in the present sample and those in Boroson et al. (2011) with measured MIR class and age. Error bars are from Annibali et al. (2007) and Table 2. The horizontal dotted lines indicate the range of ages found in the literature. Symbols as in Fig. 9.

Fig. 10 shows the relation between the gas luminosity, measured relative to the stellar component, and stellar age. Expectations would suggest that young galaxies, where SF could have enhanced gas consumption and winds, should contain a smaller amount of hot emitting gas relative to older systems, which had more time to rebuild their ISM (Mackie & Fabbiano 1998; Sansom et al. 2006). The time sequence discussed by Brassington et al. (2007) shows the expected X-ray emission at different phases of a merging event between gas-rich galaxies. Gas-poor systems should follow the same trend, although the outcome is most likely less evident (see Trinchieri et al. 2008 for an example).

The relation between hot gas content and luminosity-weighted stellar age is not a simple one, and results have been differently interpreted (see discussion in Boroson et al. 2011, Memola et al 2009, Kim & Fabbiano 2010, Kim, Fabbiano & Pipino 2012). Age-related X-ray signatures are found in specific areas (such as the ring in NGC 1291; Luo et al. 2012), in the X-ray luminosity function of the binary population (Kim & Fabbiano 2010; Lehmer et al. 2014) and in the metal abundances ratios of the hot ISM (Kim et al. 2012). However, inspection of Fig. 10 is not encouraging: even disregarding the intrinsic uncertainties in the determination of ages (which could be very large in specific cases), there is no

obvious trend suggesting a preference of larger gas content in older systems. We also notice that there is very little relation between the luminosity-weighted ages derived and the signatures of recent activity in the MIR classification or in the outer UV structures.

5 SUMMARY AND CONCLUSIONS

We present new X-ray observations for 12 ETGs with *XMM–Newton* and *Swift*. Only one, NGC 2974, was previously observed in X rays (a short, heavily contaminated observation of NGC 2685 also exists). 10 galaxies in our sample have a measured MIR spectrum from *Spitzer*-IRS data, which indicates a passively to moderately post-star-forming activity, without a contribution from an active AGN. All galaxies have FUV images from either *GALEX* or these new *Swift*-UVOT data. Many of the galaxies are S0s, in spite of the original classification from RSA. Several show kinematical signatures of recent accretion/interaction events and/or peculiar morphological structures observed in the UV as rings/arms or polar rings which again point at past and/or ongoing interaction/accretion episodes. The MIR nuclear properties further support this picture showing the presence of PAH in the nucleus of several galaxies in the sample.

We analysed their X-ray luminosities and spectral properties as well as their optical and FUV morphologies derived from *Swift*-UVOT. For galaxies with morphological signatures of interaction/accretion, UVOT observations show the emergence of ring/arm-like structures becoming more prominent at shorter, UV wavelengths, highlighting the different stellar mix that produces the observed luminosities in different spectral ranges. The details of the UVOT analysis and results will be given in a future paper.

All galaxies have been detected in X-ray, and hot gas in about half of them, with luminosities exceeding 10^{39} erg s^{-1} and up to 10^{40} erg s^{-1}.

We have started a comparison between global X-ray luminosities, MIR classes and UV features, in order to understand whether and how low-level SF activity at large scale, current or relatively recent, may influence the X-ray emission. Observations suggest that the mechanism generating the large-scale SF may also induce different forms of activity, SF and/or AGN, in the galaxy nucleus (Rampazzo et al. 2011). However, when compared to the X-ray properties, we find little evidence of any influence of the SF activity (albeit at very low level in these systems) on the global X-ray properties, either LMXB or gas components. We confirm this by doubling the sample with the ETGs analysed by the Boroson et al. (2011) with measured MIR properties. These have high-quality X-ray data obtained with deep *Chandra* observations, and have a more reliable measure of the different components in each object. While evidence is accumulating that locally, at the sites of recent SF witnessed by e.g. excess UV emission, there could be an effect on the X-ray emission, there seems to be no evidence of a measurable global effect.

In particular our new X-ray observations confirm earlier results (cf. Memola et al 2009; see also discussion in Boroson et al. 2011 and references therein) that there is little evidence of a relation between the global hot gas content and the luminosity-weighted age of the system, measured from the stellar population in the nuclear region, modelling the optical Lick line-strength indices. In many cases, we found large discrepancies in the published estimates of the ages (Fig. 10), due to different assumptions, line-strength corrections and index modelling, that prevent a reliable study of the relation between the X-ray content to the galaxy age so determined.

To better explore this aspect, we are planning to add the X-ray information that we now have in order to better exploit the predictive power of a set of SPH simulations with chemo-photometric implementation already applied by Mazzei et al. (2014a) to NGC 1533 (see also Trinchieri et al. 2012, for a first attempt at this method).

Mazzei et al. (2014a) developed a set of SPH simulations with chemo-photometric implementation specifically geared to NGC 1533, that suggest that this galaxy is the result of a major merging (2:1).

This approach is quite demanding since it requires the determination of the galaxy spectral energy distribution (SED) on a wide wavelength range in order to fix the appropriate SPH simulation and its snapshot corresponding to the current galaxy properties along the galaxy evolution.

The comparison, together with the simultaneous fit of the galaxy total magnitude, its morphology, 2D kinematics, X-ray properties and so on, will further constrain the epoch at which the galaxy is observed, based on information on specific evolution provided by the simulation (see, e.g. Mazzei et al. 2014a; Mazzei, Marino & Rampazzo 2014b).

ACKNOWLEDGEMENTS

We thank an anonymous referee for a very careful reading of the manuscript. Based on observations obtained with *XMM–Newton*, an ESA science mission with instruments and contributions directly funded by ESA. We acknowledge partial financial support from contract ASI-INAF I/009/10/0; INAF PRIN 2011: Galaxy Evolution with the VLT Survey Telescope (VST). ASI-INAF I/016/07/0. This research has made use of the NASA/ IPAC Infrared Science Archive, which is operated by the Jet Propulsion Laboratory, California Institute of Technology, under contract with the National Aeronautics and Space Administration.

REFERENCES

Annibali F., Bressan A., Rampazzo R., Zeilinger W. W., 2006, A&A, 445, 79
Annibali F., Bressan A., Rampazzo R., Zeilinger W. W., Danese L., 2007, A&A, 463, 455
Annibali F., Bressan A., Rampazzo R., Zeilinger W. W., Vega O., Panuzzo P., 2010, A&A, 519, A40
Bieging J. H., 1978, A&A, 64, 23
Boroson B., Kim D.-W., Fabbiano G., 2011, ApJ, 729, 12
Brassington N. J., Ponman T. J., Read A. M., 2007, MNRAS, 377 1439
Bressan A. et al., 2006, ApJ, 639, L55
Brown M. J. I., Januzzi B. T., Floyd D. J. E., Mould J. R., 2011, ApJ, 731, L41
Burrows D. N. et al., 2005, Space Sci. Rev., 120, 165
Capaccioli M., Piotto G., Rampazzo R., 1988, AJ 96, 487
Carollo M., Danziger I. J., 1994, MNRAS, 270, 523
Citterio O. et al., 1994, in Hoover R. B., Walker A. B., eds, Proc. SPIE Conf. Ser. Vol. 2279, Advances in Multilayer and Grazing Incidence X-Ray/EUV/FUV Optics. SPIE, Bellingham, p. 480
Colbert E. J. M., Heckman T. M., Ptak A. F., Strickland D. K., Weaver K. A., 2004, ApJ, 602, 231
Condon J. J., Cotton W. D., Greisen E. W., Yin Q. F., Perley R. A., Taylor G. B., Broderick J. J., 1998, AJ, 115, 169
Demoulin-Ulrich M.-H., Butcher H. R., Boksenberg A., 1984, ApJ, 285, 527
David L. P., Jones C., Forman W., Vargas I. M., Nulsen P., 2006, ApJ, 653 207
Emsellem E. et al., 2011, MNRAS, 414, 888

Forman W., Schwarz J., Jones C., Liller W., Fabian A. C., 1979, ApJ, 234, L27
Forman W., Jones C., Tucker W., 1985, ApJ, 293, 102
Franx M., van Gorkom J. H., de Zeew T., 1994, ApJ, 436, 642
Freeman P., Doe S., Siemiginowska A., 2001, in Starck J.-L., Murtagh F. D., eds, Proc. SPIE Conf. Ser. Vol. 4477, Astronomical Data Analysis. SPIE, Bellingham, p. 76
Gallagher J. S., Faber S. M., Balick B., 1975, ApJ, 202, 7
Garcììa-Barreto J. A., Moreno E., 2000, ApJ, 529, 832
Gehrels N. et al., 2004, ApJ, 611, 1005
Goudfrooij P., 1994, PhD thesis, Univ. Amsterdam
Grevesse N., Sauval A. J., 1998, Space Sci. Rev., 85, 161
Ho L. C., Filippenko A. V., Sargent W. L. W., 1997, ApJ, 487, 568
Ho L. C., Zhao-Yu L., Barth A. J., Seigar M. S., Peng C. Y., 2011, ApJS, 197, 21
Hoversten E. A. et al., 2011, AJ, 141, 205
Jansen F. et al., 2001, A&A, 365, L1
Jeong H. et al., 2009, MNRAS, 398, 2028
Józsa G. I. G., Oosterloo T. A., Morganti R., Klein U., Erben T., 2009, A&A, 494, 489
Kaneda H., Honaka T., Sakon L., Kitayama T., Okada Y., Suzuki T., 2008, ApJ, 684, 270
Kilborn V. A. Koribalski B. S., Forbes D. A., Barnes D. G., Musgrave R. C., 2005, MNRAS, 356, 77
Kim D.-W., 1989, ApJ, 346, 653
Kim D.-W., Fabbiano G., 2004, ApJ, 611, 846
Kim D.-W., Fabbiano G., 2010, ApJ, 721, 1523
Kim D.-W. Fabbiano G., Pipino A., 2012, ApJ, 751, 38
Laurikainen E., Salo H., Buta R., Knapen J. H., 2011, MNRAS, 418, 1452
Lehmer B. D. et al., 2014, ApJ, 789, 52
Longhetti M., Bressan A., Chiosi C., Rampazzo R., 1999, A&A, 345, 419
Longhetti M., Bressan A., Chiosi C., Rampazzo R., 2000, A&A, 353, 917
Luo B. et al., 2012, ApJ, 749, 130
Mackie G., Fabbiano G., 1998, AJ, 115, 514
Malin D. F., Carter D., 1983, ApJ, 274, 534
Mapelli M., Rampazzo R., Marino A., 2015, A&A, 575, A16
Marino A. et al., 2011a, MNRAS, 411, 311
Marino A., Bianchi L., Rampazzo R., Thilker D. A., Annibali F., Bressan A., Buson L. M., 2011b, ApJ, 736, 154
Mazzei P., Marino A., Rampazzo R., Galletta G., Bettoni D., 2014a, Adv. Space Res., 53, 950
Mazzei P., Marino A., Rampazzo R., 2014b, ApJ, 782, 53
Memola E., Trinchieri G., Wolter A., Focardi P., Kelm B., 2009, A&A, 497, 359
Morelli L. et al., 2008, MNRAS, 389, 341
Moretti A. et al., 2005, in Siegmund O. H. W., ed., Proc. SPIE Conf. Ser. Vol. 5898, UV, X-Ray, and Gamma-Ray Space Instrumentation for Astronomy XIV. SPIE, Bellingham, p. 360
Nanni A., Bressan A., Marigo P., Girardi L., 2013, MNRAS, 434, 2390
Panuzzo P., Rampazzo R., Bressan A., Vega O., Annibali F., Buson L. M., Clemens M. S., Zeilinger W. W., 2011, A&A, 528, A10
Pizzella A. et al., 1997, A&A, 323, 349
Rampazzo R., Annibali F., Bressan A., Longhetti M., Padoan F., Zeilinger W. W., 2005, A&A, 433, 497
Rampazzo R. et al., 2011, Ap&SS, 335, 201
Rampazzo R., Panuzzo P., Vega O., Marino A., Bressan A., Clemens M. S., 2013, MNRAS, 432, 374
Rampazzo R., Vega O., Bressan A., Clemens M. S., Marino A., Panuzzo P., 2014, A&A, 565, A50
Ryan-Weber E., Webster R., Bekki K., 2003, Astrophys. Space Sci. Libr., 281, 223
Sansom A. E., O'Sullivan E., Forbes D. A., Proctor R. N., Davis D. S., 2006, MNRAS, 370, 1541
Schechter P. L., Gunn J. E., 1978, AJ, 83, 1360
Schweizer F., van Gorkom J. H., Seitzer P., 1989. ApJ, 338, 770
Scorza C., Bender R., Wilkelmann C., Capaccioli M., Macchetto D. F., 1998, A&AS, 131, 265
Serra P., Oosterloo T. A., 2010, MNRAS, 401, L29
Strüder L. et al., 2001, A&A, 365, L18
Temi P., Brighenti F., Mathews W. G., 2009, ApJ, 707 890
Trager S. C., Faber S. M., Worthey G., Gonzlez J. J., 2000a, AJ, 119, 1645
Trager S. C., Faber S. M., Worthey G., Gonzlez J. J., 2000b, AJ, 120, 165
Trinchieri G., Fabbiano G., 1985, ApJ, 296, 447
Trinchieri G., Rampazzo R., Chioosi C., Grützbauch R., Marino A., Tantalo R., 2008, A&A, 489, 85
Trinchieri G., Marino A., Mazzei P., Rampazzo R., Wolter A., 2012, A&A, 545, 140
Tully R. B., 1988, Nearby Galaxies Catalog. Cambridge Univ. Press, Cambridge
Turner M. J. L. et al., 2001, A&A, 365, L27
Ulrich M.-H., 1975, PASP, 87, 965
Vega O., Bressan A., Panuzzo P., Rampazzo R., Clemens M. S., Granato G. L., Buson L., Silva L., Zeilinger W. W., 2010, ApJ, 721, 1090
Vollmer B. P., 2013, in Oswalt T. D., Keel W. C., eds, Stars and Stellar Systems Vol. 6. Springer, Dordrecht, p. 207
Werk J. K., 2010, AJ, 139, 279
White R. E., III Sarazin C. L., Kulkarni S. R., 2002, ApJ, 571, L23
Worthey G., 1994, ApJS, 95 107

This paper has been typeset from a TEX/LATEX file prepared by the author.